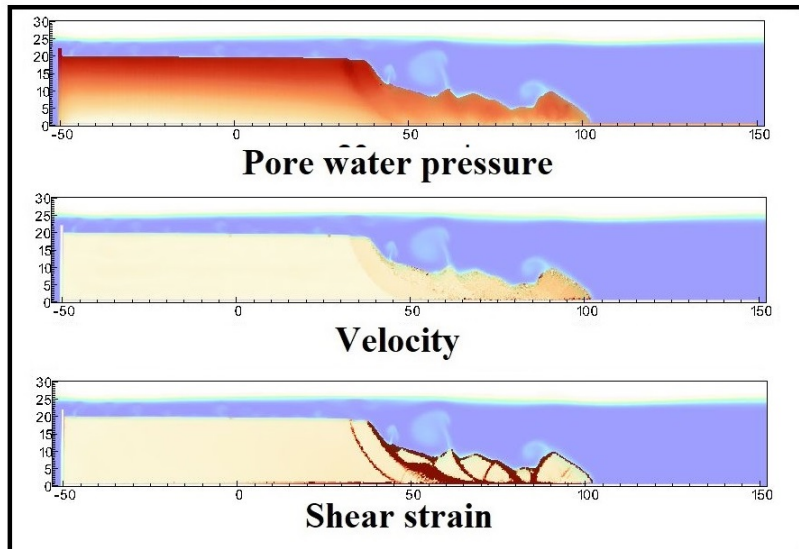


- 1 Graphical Abstract
- 2 MPMICE: A hybrid MPM-CFD model for simulating coupled problems in porous media. Application to earthquake-induced submarine landslides
- 3 Quoc Anh Tran, Gustav Grimstad, Seyed Ali Ghoreishian Amiri



Application to earthquake-induced submarine landslide

₆ Highlights

₇ **MPMICE: A hybrid MPM-CFD model for simulating coupled prob-**
₈ **lems in porous media. Application to earthquake-induced subma-**
₉ **rine landslides**

₁₀ Quoc Anh Tran, Gustav Grimstad, Seyed Ali Ghoreishian Amiri

- ₁₁ • MPMICE is introduced for multiphase flow in porous media.
- ₁₂ • Material Point method allows to model large deformation of non-isothermal
- ₁₃ porous media.
- ₁₄ • ICE (compressible multi-material CFD formulation) allows ~~to stabilize~~
- ₁₅ stabilizing pore water pressure and turbulent flow.
- ₁₆ • MPMICE is validated and apply to simulate the earthquake-induced
- ₁₇ submarine landslide.

¹⁸ MPMICE: A hybrid MPM-CFD model for simulating
¹⁹ coupled problems in porous media. Application to
²⁰ earthquake-induced submarine landslides

²¹ Quoc Anh Tran^a, Gustav Grimstad^a, Seyed Ali Ghoreishian Amiri^a

^a*Norwegian University of Science and Technology, , Trondheim, 7034, Norway*

²² Abstract

²³ In this paper, we describe a soil-fluid-structure interaction model that com-
²⁴ bines soil mechanics (saturated sediments), fluid mechanics (seawater or air),
²⁵ and solid mechanics (structures). The formulation combines the Material
²⁶ Point Method, which models large deformation of the porous media and the
²⁷ structure, with the Implicit Continuous-fluid Eulerian, which models com-
²⁸ plex fluid flows. We validate the model and simulate the whole process of
²⁹ earthquake-induced submarine landslides. We show that this model captures
³⁰ complex interactions between saturated sediment, seawater, and structure,
³¹ so we can use the model to estimate the impact of potential submarine land-
³² slides on offshore structures.

³³ *Keywords:*

³⁴ Material Point Method, MPMICE, submarine landslide.

35	Contents	
36	Nomenclature	4
37	Introduction	6
38	Theory and formulation	8
39	Assumptions	8
40	Governing equations	9
41	Constitutive soil model	11
42	Turbulent model	12
43	Frictional force for soil-structure interaction	12
44	Momentum and Energy exchange model	13
45	Solving momentum and energy exchange with an implicit solver	14
46	Equation of state for fluid phases	16
47	Numerical implementation	17
48	Interpolation from Solid Particle to Grid	18
49	Compute equation of state for fluid phase	20
50	Compute face-centered velocity Compute cell face velocity	20
51	Compute face-centered temperature Compute cell face temperature	21
52	Compute fluid pressure (implicit scheme)	22
53	Compute viscous shear stress term of the fluid phase	22
54	Compute nodal internal temperature of the solid phase	23
55	Compute and integrate acceleration of the solid phase	23
56	Compute Lagrangian value (mass, momentum and energy)	23
57	Compute Lagrangian specific volume of the fluid phase	25
58	Compute advection term and advance in time	26
59	Interpolate from cell to node of the solid phase	26
60	Update the particle variables	27
61	Numerical examples	27
62	Fluid Flow through isothermal porous media	28
63	Isothermal consolidation	29
64	Thermal induced cavity flow	30
65	Underwater debris flow	31
66	Validation of soil response to the seismic loading	35
67	Earthquake-induced submarine landslides	38

68	Conclusions	43
69	Acknowledgements	44
70	Appendix: Equation derivation	44
71	Evolution of porosity	45
72	Momentum conservation	45
73	Energy conservation	46
74	Advanced Fluid Pressure	47
75	Momentum and Energy exchange with an implicit solver	48

⁷⁶ **Nomenclature**

General variables

<u>Variable</u>	<u>Dimensions</u>	<u>Description</u>
V	$[L^3]$	Representative volume
n		Porosity
σ	$[ML^{-1}t^{-2}]$	Total stress tensor
Δt	$[t]$	Time increment
\mathbf{b}	$[ML^1t^{-2}]$	Body force
c_v	$[L^2t^{-2}T^{-1}]$	Constant volume specific heat
f_d	$[MLt^{-2}]$	Drag forces in momentum exchange term
f^{int}	$[MLt^{-2}]$	Internal forces
f^{ext}	$[MLt^{-2}]$	External forces
q_{fs}	$[MLt^{-2}]$	Heat exchange term
S		Weighting function
∇S		Gradient of weighting function

⁷⁷

Solid phase

<u>Variable</u>	<u>Dimensions</u>	<u>Description</u>
m_s	$[M]$	Solid mass
ρ_s	$[ML^{-3}]$	Solid density
ϕ_s		Solid volume fraction
$\bar{\rho}_s$	$[ML^{-3}]$	Bulk Solid density
\mathbf{x}_s	$[L]$	Solid Position vector
\mathbf{U}_s	$[Lt^{-1}]$	Solid Velocity vector
\mathbf{a}_s	$[Lt^{-2}]$	Solid Acceleration vector
σ'	$[ML^{-1}t^{-2}]$	Effective Stress tensor
ϵ_s		Strain tensor
e_s	$[L^2t^{-2}]$	Solid Internal energy per unit mass
T_s	$[T]$	Solid Temperature
\mathbf{F}_s		Solid Deformation gradient
V_s	$[L^3]$	Solid Volume

Fluid phase

<u>Variable</u>	<u>Dimensions</u>	<u>Description</u>
m_f	[M]	Fluid mass
ρ_f	[ML ⁻³]	Fluid density
ϕ_f		Fluid volume fraction
$\bar{\rho}_f$	[ML ⁻³]	Bulk Fluid density
\mathbf{U}_f	[Lt ⁻¹]	Fluid Velocity vector
$\boldsymbol{\sigma}_f$	[ML ⁻¹ t ⁻²]	Fluid stress tensor
p_f	[ML ⁻¹ t ⁻²]	Fluid isotropic pressure
$\boldsymbol{\tau}_f$	[ML ⁻¹ t ⁻²]	Fluid shear stress tensor
e_f	[L ² t ⁻²]	Fluid Internal energy per unit mass
T_f	[T]	Fluid Temperature
v_f	[L ³ /M]	Fluid Specific volume $\frac{1}{\rho_f}$
α_f	[1/T]	Thermal expansion
μ	[ML ⁻¹ t ⁻¹]	Fluid viscosity
V_f	[L ³]	Fluid Volume

Superscript

<u>Variable</u>	<u>Dimensions</u>	<u>Description</u>
n		Current time step
L		Lagrangian values
$n + 1$		Next time step

Subscript

c	Cell-centered quantity
p	Particle quantity
i	Node quantity
FC	Face-centered Cell face quantity
L, R	Left and Right cell faces

79 **Introduction**

80 Many geological natural processes and their interactions with man-made
81 structures are influenced by soil-fluid-structure interactions. The prediction
82 of these processes requires a tool that can capture complex interactions
83 between soil, fluid, and structure, such as the process of submarine land-
84 slides. Indeed, The offshore infrastructure as well as coastal communities
85 may be vulnerable to submarine landslides. Submarine landslides contain
86 three stages: triggering, failure, and post-failure. Erosion or earthquakes can
87 trigger slope failures in the first stage. Following the failure, sediments move
88 quickly after the post-failure stage. In other words, solid-like sediments will
89 behave like a fluid after failure. This phase transition makes the simulation
90 of submarine landslides a challenging task.

91

92 Due to this phase transition, submarine landslide can be modeled by ei-
93 ther the Computational Fluid Dynamics (CFD) or the particle-based meth-
94 ods. For simulating submarine slides, CFD methods solve governing equa-
95 tions in a full-Eulerian framework [1, 2, 3, 4] with interface capturing tech-
96 niques. While CFD can handle complex flows (such as turbulent flows), it
97 cannot account for the triggering mechanism of submarine landslides because
98 it is not ~~straightforward~~ straightforward to consider 'soil constitutive laws' of
99 sediment materials in the Eulerian framework. In contrast, particle-based
100 methods can overcome this problem by using the Lagrangian framework.
101 These methods have been extensively used to simulate landslides, like Mate-
102 rial Point Method (MPM) [5], Smooth Particle Hydro Dynamics [6], Particle
103 Finite Element Method [7], or Coupled Eulerian Lagrangian Method [8]. For
104 simplicity, these simulations adopt total stress analysis which neglects the
105 pore pressure development which is key factor triggering slope failures.

106

107 Recent developments in particle-based methods model the coupling of
108 fluid flows in porous media by sets of Lagrangian particles. For the MPM
109 family, it is the double-point MPM ([9, 10, 11]) where fluid particles and
110 solid particles are overlapped in a single computational grid. Even if fluid
111 flows are considered, particle-based methods have numerical instability in
112 modeling the fluid flow, which requires additional numerical treatments such
113 as the B-bar method [9], null-space filter [12], or least square approximation
114 [13, 14]. Indeed, CFD is a more optimal option for complex fluid flows
115 especially dealing with large distortions of continuum fluid media. Therefore,

116 it could be ideal to combine the CFD with particle-based methods. More than
 117 50 particle-based methods have been developed to solve large deformations
 118 of solids over the last two decades [15], but the MPM appears to be the
 119 best candidate for coupling with the CFD. Because MPM incorporates a
 120 stationary mesh during computation, just like CFD. As such, both MPM
 121 and CFD can be coupled naturally in a unified computational mesh.



Figure 1: Interaction between soil-fluid-structure

122

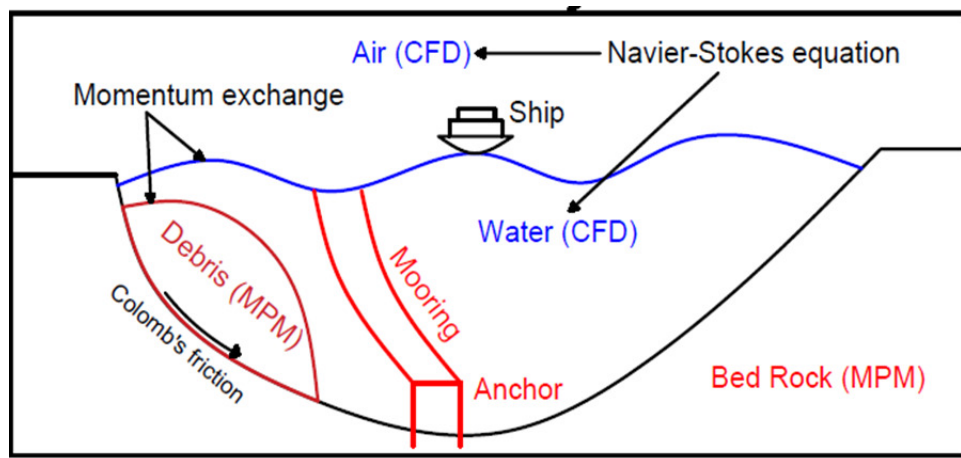


Figure 2: Coupling of soil-water-structure interaction using MPMICE

123 A numerical method for simulating soil-fluid-structure interaction (Figure
124 1) involving large deformations, is presented in this work in order to simu-
125 late the interaction between sediment (soil), seawater (fluid) and offshore
126 structures (structure) namely MPMICE (Figure 2). In the MPMICE, the
127 Material Point Method (MPM) is coupled with the Implicit Continuous Eu-
128 lerian (ICE). The MPM method is a particle method that allows the porous
129 soil to undergo arbitrary distortions. The ICE method, on the other hand,
130 is a conservative finite volume technique with all state variables located at
131 the cell center (temperature, velocity, mass, pressure). An initial technical
132 report [16] at Los Alamos National Laboratory provided the theoretical and
133 algorithmic foundation for the MPMICE, followed by the MPMICE devel-
134 opment and implementation in the high-performance Uintah computational
135 framework for simulating fluid-structure interactions [17]. This paper pri-
136 marily contributes ~~further~~ further to the development of the MPMICE for
137 analyzing the **soil**-fluid-structure interaction, since sediment should be con-
138 sidered as a porous media (soil) and not as a solid to capture the evolution
139 of the pore water pressure. Baumgarten et al. [18] made the first attempt
140 at coupling the Finite Volume Method with the MPM for the simulation of
141 soil-fluid interaction. In contrast to the mentioned work, we use implicit time
142 integration for the multi phase flows instead of explicit time integration for
143 the single-phase flow.

144 **Theory and formulation**

145 This section lay out the theoretical framework for the MPMICE model.
146 We use the common notation of the continuum ~~meehaniees~~ mechanics with
147 vector and tensor denoted simply by using bold font and scalar denoted by
148 using normal font. The notation are shown in Nomenclature.

149 *Assumptions*

150 The following assumptions are made for the MPMICE model.

- 151 1. Solid phases (MPM) are described in a Lagrangian formulation while
152 fluid phases (ICE) are described in an Eulerian formulation in the
153 framework of continuum mechanics and mixture theory.
- 154 2. Solid grains are incompressible while the fluid phases are compressible.
155 Solid's thermal expansion is negligible.
- 156 3. There is no mass exchange between solid and fluid phases.
- 157 4. Terzaghi's effective stress is valid.

158 *Governing equations*

159 A representative element volume Ω is decomposed by two domains: solid
160 domains Ω_s and fluid domains Ω_f . Then, all domains are homogenized
161 into two overlapping continua. Considering the volume fraction of solid
162 $\phi_s = \Omega_s/\Omega$ and fluid $\phi_f = \Omega_f/\Omega$ with the true (or Eulerian) porosity
163 $n = \sum \phi_f$ of the representative element volume, the average density of solid
164 and fluid phases are defined as:

165

$$\bar{\rho}_s = \phi_s \rho_s, \quad \bar{\rho}_f = \phi_f \rho_f \quad (1)$$

166 The mass of solid and fluid phases are:

167

$$m_s = \int_{\Omega_s} \rho_s dV = \bar{\rho}_s V, \quad m_f = \int_{\Omega_f} \rho_f dV = \bar{\rho}_f V \quad (2)$$

168 Reviewing the Terzaghi's effective stress concept for the saturated porous
169 media, the total stress $\boldsymbol{\sigma}$ is calculated by:

170

$$\boldsymbol{\sigma} = \boldsymbol{\sigma}' - p_f \mathbf{I} \quad (3)$$

171 The balance equations are derived based on the mixture theory. The rep-
172 resentative thermodynamic state of the fluid phases are given by the vector
173 $[m_f, \mathbf{U}_f, e_f, T_f, v_f]$ which are mass, velocity, internal energy, temperature,
174 specific volume. The representative state of the solid phases are given by the
175 vector $[m_s, \mathbf{U}_s, e_s, T_s, \boldsymbol{\sigma}', p_f]$ which are mass, velocity, internal energy, temper-
176 ature, effective stress and pore water pressure. The derivation is presented
177 in detail in the Appendix.

178

179 Mass Conservation

180 The mass balance equations for both fluid (e.g., water, air) and solid phases
181 are:

182

$$\frac{1}{V} \frac{\partial m_f}{\partial t} + \nabla \cdot (m_f \mathbf{U}_f) = 0, \quad \frac{1}{V} \frac{D_s m_s}{Dt} = 0 \quad (4)$$

183 Solving the mass balance equation leads to:

$$\frac{D_s n}{Dt} = \phi_s \nabla \cdot \mathbf{U}_s \quad (5)$$

184

185 Momentum Conservation

¹⁸⁶ The momentum balance ~~equation-equations~~ for the fluid phases (e.g., water,
¹⁸⁷ air) are:

$$\frac{1}{V} \left[\frac{\partial(m_f \mathbf{U}_f)}{\partial t} + \nabla \cdot (m_f \mathbf{U}_f \mathbf{U}_f) \right] = -\phi_f \nabla p_f + \nabla \cdot \boldsymbol{\tau}_f + \bar{\rho}_f \mathbf{b} + \sum \mathbf{f}_d \quad (6)$$

¹⁸⁸ The momentum balance ~~equation-equations~~ for the solid phases are:

$$\frac{1}{V} \frac{D_s(m_s \mathbf{U}_s)}{Dt} = \nabla \cdot (\boldsymbol{\sigma}') - \phi_s \nabla p_f + \bar{\rho}_s \mathbf{b} + \sum \mathbf{f}_{fric} - \sum \mathbf{f}_d \quad (7)$$

189 Energy Conservation

¹⁹⁰ The internal energy balance ~~equation-equations~~ for the fluid phases (e.g.,
¹⁹¹ water, air) are:

$$\frac{1}{V} \left[\frac{\partial(m_f e_f)}{\partial t} + \nabla \cdot (m_f e_f \mathbf{U}_f) \right] = -\bar{\rho}_f p_f \frac{D_f v_f}{Dt} + \boldsymbol{\tau}_f : \nabla \mathbf{U}_f + \nabla \cdot \mathbf{q}_f + \sum q_{sf} \quad (8)$$

¹⁹² The internal energy balance ~~equation-equations~~ for the solid phase ~~is~~are:

$$\frac{m_s}{V} c_v \frac{D_s(T_s)}{Dt} = \boldsymbol{\sigma}' : \frac{D_s(\boldsymbol{\epsilon}_s^p)}{Dt} + \nabla \cdot \mathbf{q}_s - \sum q_{sf} \quad (9)$$

¹⁹³ where c_v is the specific heat at constant volume of the solid materials.

¹⁹⁴ Closing the systems of equations, the following additional models are needed:

¹⁹⁵ (1) A constitutive equation to describe the stress - strain behaviour of solid
¹⁹⁶ phase (computing effective stress $\boldsymbol{\sigma}'$).
¹⁹⁷ (2) Optional turbulent model to compute the viscous shear stress $\boldsymbol{\tau}_f$.
¹⁹⁸ (3) Frictional forces \mathbf{f}_{fric} for the contact for soil-structure interaction be-
¹⁹⁹ tween solid/porous materials with the friction coefficient μ_{fric} .
²⁰⁰ (4) Exchange momentum models (computing drag force \mathbf{f}_d) for interaction
²⁰¹ between materials.
²⁰² (5) Energy exchange models (computing temerature exhange term q_{sf}) for
²⁰³ interaction between materials.
²⁰⁴ (6) An equation of state to establish relations between thermodynamics vari-
²⁰⁵ ables of each fluid materials $[P_f, \bar{\rho}_f, v_f, T_f, e_f]$.

208 Four thermodynamic relations for the equation of states are:

$$\begin{aligned} e_f &= e_f(T_f, v_f) \\ P_f &= P_f(T_f, v_f) \\ \phi_f &= v_f \bar{\rho}_f \\ 0 &= n - \sum_{f=1}^{N_f} v_f \bar{\rho}_f \end{aligned} \quad (10)$$

209 *Constitutive soil model*

210 As a result of the explicit MPM formulation, we can derive the consti-
 211 tutive law in the updated Lagrangian framework of "small strain - large
 212 deformation". Therefore, the rotation of the particles (representative ele-
 213 ment volume) is manipulated by rotating the Cauchy stress tensor. First,
 214 the deformation gradient is decomposed into the polar rotation tensor \mathbf{R}_s^{n+1}
 215 and ~~sketch~~-stretch tensor \mathbf{V}_s^{n+1} as:

$$\mathbf{F}_s^{n+1} = \mathbf{V}_s^{n+1} \mathbf{R}_s^{n+1} \quad (11)$$

216 Then, before calling the constitutive model, the stress and strain rate tensor
 217 are rotated to the reference configuration as:

$$\boldsymbol{\sigma}'^{n*} = (\mathbf{R}_s^{n+1})^T \boldsymbol{\sigma}'^{n*} \mathbf{R}_s^{n+1} \quad (12)$$

$$\delta\boldsymbol{\epsilon}^{n*} = (\mathbf{R}_s^{n+1})^T \delta\boldsymbol{\epsilon}_s^{n*} \mathbf{R}_s^{n+1} \quad (13)$$

219 Using the constitutive model with the input tensors $\boldsymbol{\sigma}'^{n*}, \delta\boldsymbol{\epsilon}^{n*}$ to compute
 220 the Cauchy stress tensor at the advanced time step $\boldsymbol{\sigma}'^{n+1*}$ then rotating it
 221 back to current configuration as:

$$\boldsymbol{\sigma}'^{n+1} = \mathbf{R}_s^{n+1} \boldsymbol{\sigma}'^{n+1*} (\mathbf{R}_s^{n+1})^T \quad (14)$$

222 In this paper, we adopt the hyper-elastic Neo Hookean model for the structure
 223 materials and additionally Mohr-Coulomb failure criteria for the soil (porous
 224 media) materials. The Cauchy stress of the hyper-elastic Neo Hookean model
 225 can be written as:

$$\boldsymbol{\sigma}' = \frac{\lambda \ln(J)}{J} + \frac{\mu}{J} (\mathbf{F} \mathbf{F}^T - \mathbf{J}) \quad (15)$$

226 where λ and μ are bulk and shear modulus ad J is the determinant of the
 227 deformation gradient \mathbf{F} . And the yield function f and flow potentials g of

²²⁸ the Mohr-Coulomb can be written as:

$$\begin{aligned} f &= \sigma'_1 - \sigma'_3 - 2c' \cos(\phi') - (\sigma'_1 + \sigma'_3) \sin(\phi') \\ g &= \sigma'_1 - \sigma'_3 - 2c' \cos(\psi') - (\sigma'_1 + \sigma'_3) \sin(\psi') \end{aligned} \quad (16)$$

²²⁹ where the c' , ϕ' and ψ' are cohesion and friction angle and dilation angle. σ'_1
²³⁰ and σ'_3 are maximum and minimum principal stress.

²³¹ *Turbulent model*

²³² The turbulent effect is modelled using a statistical approach namely large-
²³³ eddy simulation. In this approach, the micro-scale turbulent influence in the
²³⁴ dynamics of the macro-scale motion is computed through simple models like
²³⁵ Smagorinsky model. In the Smagorinsky ~~mode~~model, the residual stress
²³⁶ tensor is:

$$\tau_{ij} = 2\mu_{eff}(\bar{S}_{ij} - \frac{1}{3}\delta_{ij}\bar{S}_{kk}) + \frac{1}{3}\delta_{ij}\tau_{kk} \quad (17)$$

²³⁷ where the strain rate tensor is given by:..

$$\bar{S}_{ij} = \frac{1}{2}(\frac{\delta \bar{U}_i}{\delta x_j} + \frac{\delta \bar{U}_j}{\delta x_i}) \quad (18)$$

²³⁸ and the effective viscosity is sum of molecular viscosity and turbulent vis-
²³⁹ cosity $\mu_{eff} = \mu + \mu_t$ in which the turbulent viscosity μ_t is calculated by:..

$$\mu_t = (C_s \Delta)^2 \sqrt{2\bar{S}_{ij}\bar{S}_{ij}} \quad (19)$$

²⁴¹ where C_s is the Smagorinsky constant with the value of 0.1 and $\Delta = \sqrt[3]{dxdydz}$
²⁴² is the grid size that defines the subgrid length scale.

²⁴³ *Frictional force for soil-structure interaction*

²⁴⁴ MPMICE includes a contactlaw-contact law for the interaction between
²⁴⁵ soil and structure using the first Coulomb friction contact for MPM presented
²⁴⁶ by Bardenhagen et al. ([19]). The magnitude of the friction force at the
²⁴⁷ contact depends on the friction coefficient μ_{fric} and the normal force \mathbf{f}_{norm}
²⁴⁸ computed from the projection of the contact force in the normal direction.

$$\mathbf{f}_{fric} = \mu_{fric} \mathbf{f}_{norm} \quad (20)$$

²⁴⁹ The contact determines whether the soil is sliding or sticking to the structure
²⁵⁰ by comparing the friction force with the sticking force \mathbf{f}_{stick} computed from

251 the projection of the contact force in the tangent direction as:

$$\begin{aligned} & \text{if } \mathbf{f}_{fric} \geq \mathbf{f}_{stick} \text{ no sliding} \\ & \text{if } \mathbf{f}_{fric} < \mathbf{f}_{stick} \text{ sliding occurs} \end{aligned} \quad (21)$$

252 Frictional sliding between solid materials also generates dissipation and the
253 work rate generated from the sliding can be calculated as:

$$\Delta W_{friction} = \mathbf{f}_{fric} d \quad (22)$$

254 where d is the sliding distance which can be computed based on the sliding
255 velocity between two materials.

256 *Momentum and Energy exchange model*

257 Currently, the energy exchange coefficient H_{sf} is assumed to be constant
258 for the sake of simplicity. Then the energy exchange can be written as:

$$q_{sf} = H_{sf}(T_f - T_s) \quad (23)$$

259 On the other hand, the drag force can be calculated as:

$$f_d = K(\mathbf{U}_s - \mathbf{U}_f) \quad (24)$$

260 For the momentum exchange between fluid flows and porous media, we as-
261 sume that the drag force \mathbf{f}_d depends on the average grain size of the grains D_p ,
262 the porosity n , the fluid viscosity μ_f , and is proportional to the relative velocities of soil grains and fluid $(\mathbf{U}_s - \mathbf{U}_f)$. Based on recent
263 investigation of CFD simulations of fluid flow around mono- and bi-disperse
264 packing of spheres for $0.1 < \phi_s < 0.6$ and $Re < 1000$ [20]. The drag force is
265 given by:
266

$$f_d = \frac{18\phi_s(1-\phi_s)\mu_f}{D_p^2} F(\phi_s, Re)(\mathbf{U}_s - \mathbf{U}_f) \quad (25)$$

268 where Reynolds number Re are computed as:

$$Re = \frac{n\rho_f D_p}{\mu_f} \|(\mathbf{U}_s - \mathbf{U}_f)\| \quad (26)$$

269 The function $F(\phi_s, Re)$ can be calculated as:

$$F(\phi_s, Re) = F(\phi_s, 0) + \frac{0.413Re}{24(1-\phi_s)^2} \left(\frac{(1-\phi_s)^{-1} + 3\phi_s(1-\phi_s) + 8.4Re^{-0.343}}{1 + 10^{3\phi_s} Re^{-(1+4\phi_s)/2}} \right) \quad (27)$$

270 where the low Reynold coefficient $F(\phi_s, Re \rightarrow 0)$ is:

$$F(\phi_s, 0) = \frac{10\phi_s}{(1 - \phi_s)^2} + (1 - \phi_s)^2(1 + 1.5\sqrt{\phi_s}) \quad (28)$$

271 When validating the model with analytical solution, it requires to know the
 272 hydraulic conductivity \underline{K} . In such case, we convert the equation (29) to
 273 Kozeny-Carman formula by assuming $F(\phi_s, Re) = 10\phi_s/(1 - \phi_s)^2$, ~~then the~~
 274 leading to

$$\underline{f_d} = \frac{180\phi_s^2\mu_f}{D_p^2(1 - \phi_s)} (\underline{U_s} - \underline{U_f}) \quad (29)$$

275 equation Then, the draging force following the Darcy law is given by:

$$\underline{f_d} = \frac{n^2\mu_f}{\kappa} (\underline{U_s} - \underline{U_f}) \quad (30)$$

276 equation where κ being intrinsic permeability of soil which can be written
 277 as:

$$\kappa = \frac{K\mu_f}{\rho_f g} \quad (31)$$

278 equation As such, the hydraulic conductivity will be expressed as $D_p^2(1 - \phi_s)^3 / 180\mu_f\phi_s^2$.
 279 ∴

$$K = \frac{D_p^2(1 - \phi_s)^3}{180\phi_s^2\mu_f} \rho_f g \quad (32)$$

280 equation

281 *Solving momentum and energy exchange with an implicit solver*

282 The derivation of the implicit integration for the momentum exchange is
 283 presented in the Appendix's section 'Momentum and energy exchange with
 284 an implicit solver'. The linear equations for multi phases i,j=1:N has the
 285 form as:

$$\begin{vmatrix} (1 + \beta_{ij}) & -\beta_{ij} \\ -\beta_{ji} & (1 + \beta_{ji}) \end{vmatrix} \begin{vmatrix} \Delta \mathbf{U}_i \\ \Delta \mathbf{U}_j \end{vmatrix} = \begin{vmatrix} \beta_{ij}(\mathbf{U}_i^* - \mathbf{U}_j^*) \\ \beta_{ji}(\mathbf{U}_i^* - \mathbf{U}_j^*) \end{vmatrix}$$

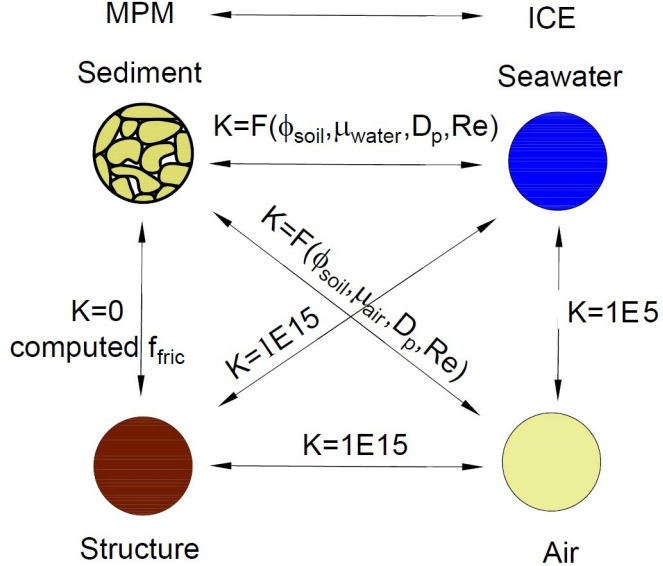


Figure 3: Momentum exchange coefficient between materials

286 where the intermediate velocity for fluid phases $f=1:N_f$ and for solid/porous
 287 phases $s=1:N_s$ can be calculated by:

$$\begin{aligned} \mathbf{U}_f^* &= \mathbf{U}_f^n + \Delta t \left(-\frac{\nabla P_f^{n+1}}{\rho_f^n} + \frac{\nabla \cdot \boldsymbol{\tau}_f^n}{\bar{\rho}_f^n} + \mathbf{b} \right) \\ \mathbf{U}_s^* &= \mathbf{U}_s^n + \Delta t \left(\frac{\nabla \cdot \boldsymbol{\sigma}'^n}{\bar{\rho}_s^n} - \frac{\nabla P_f^{n+1}}{\rho_s} + \mathbf{b} \right) \end{aligned} \quad (33)$$

288 Also, the momentum exchange coefficient can be computed at every time
 289 step as $\beta_{12} = K/\bar{\rho}_f^n$ and $\beta_{21} = K/\bar{\rho}_s^n$ with the coefficient depending on the
 290 different type of interactions (see Figure 3) as for example:

291

- 292 1. The drag force is set to zero in soil-structure interactions, and instead
 293 the frictional force is computed.
- 294 2. As a result of fluid-structure interaction, the momentum exchange coef-
 295 ficient should be extremely high (1E15) when the solid material points
 296 are considered to be zero-porosity/zero-permeability.
- 297 3. In the case of soil-fluid interaction, the drag force is calculated using
 298 the equation (29). Considering that air has a much lower viscosity than

299 water, its drag force is much lower than the drag force of water in a
 300 pore.

301 4. A momentum exchange coefficient of 1E5 is applied between multiphase
 302 flows. This value is far higher than reality [21], but it is necessary to
 303 have enough numerical stability to conduct simulations in the numerical
 304 example.

305 Similar approach applied for the energy exchange term leading to:

$$\begin{vmatrix} (1 + \eta_{ij}) & -\eta_{ij} \\ -\eta_{ji} & (1 + \eta_{ji}) \end{vmatrix} \frac{|\Delta T_i|}{|\Delta T_j|} = \frac{|\eta_{ij}(T_i^n - T_j^n)|}{|\eta_{ji}(T_j^n - T_i^n)|}$$

306 with η being the energy exchange coefficient.

307 *Equation of state for fluid phases*

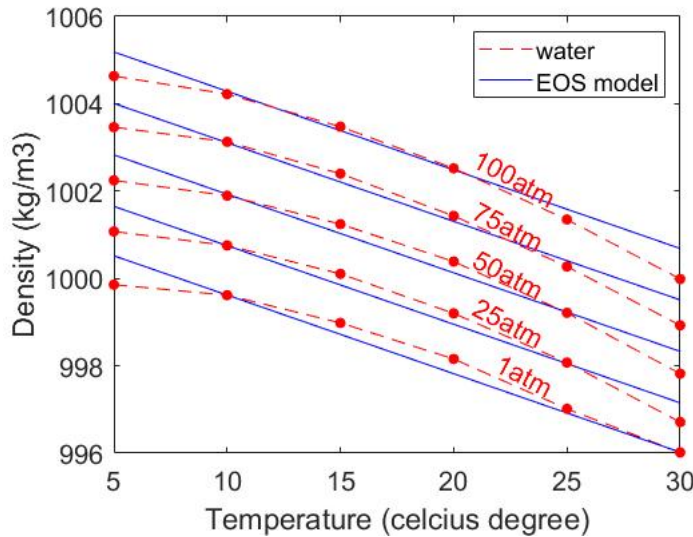


Figure 4: Equation of state of water

308 The equation of state establishes relations between thermodynamics vari-
 309 ables $[P_f, \rho_f, T_f]$. The choice of the equation of state depends on the types
 310 of the fluid materials. For example, for the air, it is possible to assume the
 311 equation of state for the perfect gas which obeys:

$$P_f = \rho_f R T_f \quad (34)$$

312 where R is the gas constant. For the water, a simple linear equation of state
 313 is in the following form:

$$P_f = P_{ref} + K_f(\rho_f - \rho_{ref} - \alpha_f(T_f - T_{ref})) \quad (35)$$

314 where reference pressure $P_{ref} = 1$ atm = 101325 Pa, reference temperature
 315 $T_{ref} = 10^\circ\text{C}$, reference density $\rho_{ref} = 999.8 \text{ kg/m}^3$, the bulk modulus of water
 316 $K_f = 2 \text{ GPa}$, and the water thermal expansion $\alpha_f = 0.18 \text{ }^\circ\text{C}^{-1}$. Equation
 317 (35) matches well with the state of the water (see Figure 4).

318 **Numerical implementation**

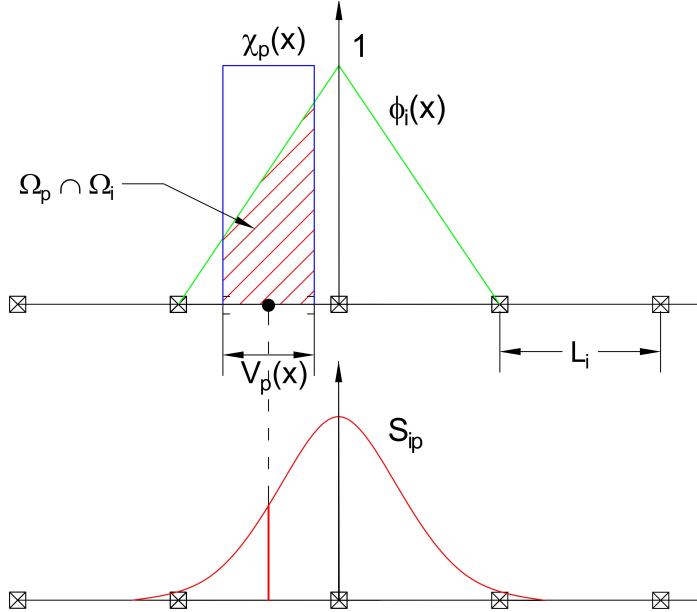


Figure 5: GIMP weighting function (red as a convolution of the linear basis shape function (green) and the charateristic-charateristic function (blue))

319 The fluid phases are discretized in the grid with the state variables stored
 320 at the centroid of the cells $[\rho_{fc}, \mathbf{U}_{fc}, T_{fc}, v_{fc}]$ while the
 321 solid phase is discretized in the particles with the state variables $[m_{sp}, \mathbf{U}_{sp}, T_{sp}, \sigma'_{sp}]$.
 322 In the Material Point Method, we use the generalized interpolation technique
 323 [22] using the weight function as a convolution of a grid shape function $N_i(\mathbf{x})$

324 in a nodal domain Ω_i and a characteristic function $\chi_p(\mathbf{x})$ in a particle domain
 325 Ω_p with the volume $V_p(\mathbf{x})$ as follows:

$$S_{ip} = \frac{1}{V_p} \int_{\Omega_i \cap \Omega_p} N_i(\mathbf{x}) \chi_p(\mathbf{x}) d\mathbf{x} \quad (36)$$

326 where the volume $V_p(\mathbf{x})$ of the material point p can be calculated as:

$$V_p = \int_{\Omega_p} \chi_p(\mathbf{x}) d\mathbf{x} \quad (37)$$

327 The ~~charateristic~~ characteristic function is the Heaviside function as $\chi_p =$
 328 1 if $\mathbf{x} \in \Omega_p$, otherwise 0 (see Figure 5). For the interpolation of the centroid
 329 of the cell, the linear basis function is used as:

$$S_{ci} = N_i(\mathbf{x}_c) \quad (38)$$

330 The time discretization are solved using the following steps:~~-~~ sidewaysfigure

331 *Interpolation from Solid Particle to Grid*

332 The nodal values of the solid state (mass, velocity, temperature, volume)
 333 are:

$$\begin{aligned} m_{si}^n &= \sum S_{ip} m_{sp} \\ \mathbf{U}_{si}^n &= \frac{\sum S_{ip} (m\mathbf{U})_{sp}^n}{m_{si}^n} \\ T_{si}^n &= \frac{\sum S_{ip} (mT)_{sp}^n}{m_{si}^n} \\ V_{si}^n &= \frac{\sum S_{ip} (mV)_{sp}^n}{m_{si}^n} \\ \boldsymbol{\sigma}_{si}^n &= \frac{\sum S_{ip} (\boldsymbol{\sigma}V)_{sp}^n}{V_{si}^n} \end{aligned} \quad (39)$$

334 The nodal internal forces is calculated by:~~-~~

$$\mathbf{f}_{si}^{int,n} = - \sum \nabla S_{ip} (\boldsymbol{\sigma}'_{sp})^n V_{sp}^n \quad (40)$$

335 The nodal external forces $f_{si}^{ext,n}$ and ~~extra momentum from contact forces~~
 336 the nodal frictional forces f_{si}^{fric} from contact between materials are com-
 337 puted here. ~~The nodal velocity and nodal temperature are applied boundary~~

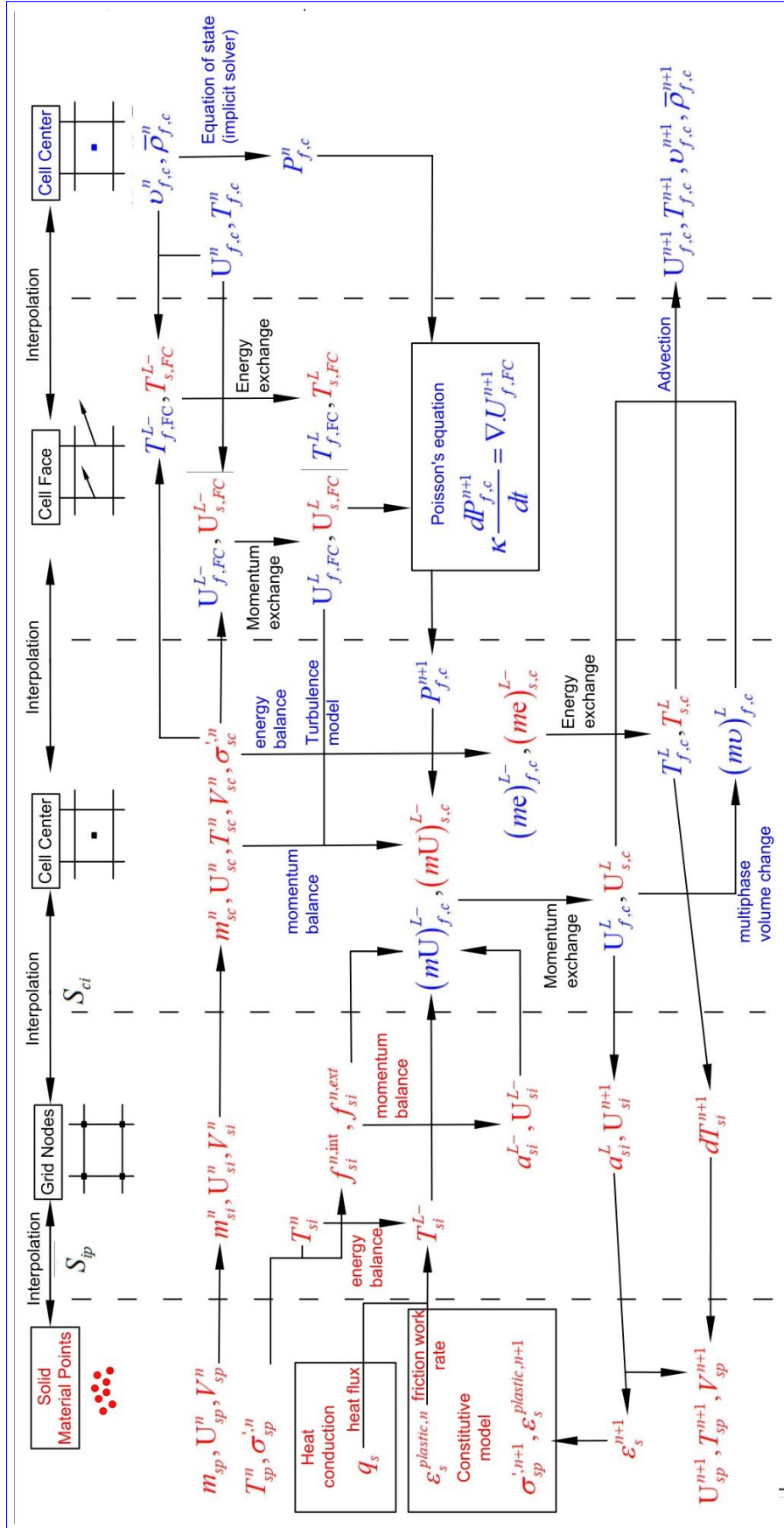


Figure 6: Numerical implementation of MP-MICE

338 **conditions.**

339 Then we compute the solid cell variables as:

$$\begin{aligned} m_{sc}^n &= \sum S_{ci} m_{si} \\ \rho_{sc}^n &= \frac{m_{sc}^n}{V} \\ \mathbf{U}_{sc}^n &= \sum S_{ci} \mathbf{U}_{si}^n \\ T_{sc}^n &= \sum S_{ci} T_{si}^n \\ V_{sc}^n &= \sum S_{ci} V_{si}^n \\ \boldsymbol{\sigma}_{sc}^n &= \sum S_{ci} \boldsymbol{\sigma}_{si}^n \end{aligned} \tag{41}$$

340 *Compute equation of state for fluid phase*

341 Considering the total fluid material The total fluid material volume of a
342 cell is:

$$V_{total} = \sum_{f=1}^{N_f} M_f v_f \tag{42}$$

343 Then we We need to find P_{eq} $P_{f,e}$ which allows each fluid materials obey their
344 equation of states $[P_f, \rho_f, v_f, T_f, e_f]$ but also allow mass of all fluid materials
345 to fill the entire the pore volume without ongoing compression or expansion
346 following the condition as follows:

$$0 = n - \sum_{f=1}^{N_f} v_f \bar{\rho}_f \tag{43}$$

347 Then, we can use he the Newton-Raphson interation to find the value of P_{eq}
348 $P_{f,e}$ which satisfies the equation (42, 43) and each equation of states of each
349 fluid materials.

350 Compute faced-centered velocity Compute cell face velocity

351 Following the derivation in the Appendix: Advanced Fluid Pressure, we
352 first compute the fluid face-centered velocity as cell face velocity as:

$$\mathbf{U}_{f,FC}^{*L} = \frac{(\bar{\rho} \mathbf{U})_{f,FC}^n}{\bar{\rho}_{f,FC}^n} + \Delta t \left(-\frac{\nabla^{FC} P_{eq}}{\rho_{f,FC}^n} \frac{\nabla^{FC} P_{f,c}^n}{\rho_{f,FC}^n} + \frac{\nabla^{FC} \cdot \boldsymbol{\tau}^n}{\bar{\rho}_{s,FC}} + \mathbf{b} \right) \tag{44}$$

353 The equation (44) is discretized in three dimension (noted that $\nabla^{FC} \cdot \boldsymbol{\tau} = 0$),
 354 for example the discretized equation in the x direction is:

$$U_{fx}^{L-} = \frac{(\bar{\rho}U)_{fx,R}^n + (\bar{\rho}U)_{fx,L}^n}{\bar{\rho}_{fx,L}^n + \bar{\rho}_{fx,R}^n} + \Delta t \left(-\frac{2(v_{fx,L}^n v_{fx,R}^n)}{v_{fx,L}^n + v_{fx,R}^n} \frac{P_{f,cx,R}^n - P_{f,cx,L}^n}{\Delta x} + b_x \right) \quad (45)$$

355 The face-centered cell face solid velocity can be calculated as:

$$\mathbf{U}_{s,FC}^{*\underline{L-}} = \frac{(\bar{\rho}\mathbf{U})_{s,FC}^n}{\bar{\rho}_{s,FC}^n} + \Delta t \left(\frac{\nabla^{FC} \cdot \boldsymbol{\sigma}_c'^n}{\bar{\rho}_{s,FC}^n} - \frac{\nabla^{FC} P_{eq} \nabla^{FC} P_{f,c}^n}{\bar{\rho}_s} + \mathbf{b} \right) \quad (46)$$

356 The equation (46) is discretized in three dimension (noted that $\nabla^{FC} \cdot \boldsymbol{\sigma}_{ij} = 0$
 357 with $i \neq j$), for example the discretized equation in the x direction is:

$$U_{sx}^{L-} = \frac{(\bar{\rho}U)_{sx,R}^n + (\bar{\rho}U)_{sx,L}^n}{\bar{\rho}_{sx,L}^n + \bar{\rho}_{sx,R}^n} + \Delta t \left(\frac{2(\sigma_{xx,R} - \sigma_{xx,L})}{(\bar{\rho}_{sx,L}^n + \bar{\rho}_{sx,R}^n) \Delta x} - \frac{P_{f,cx,R}^n - P_{f,cx,L}^n}{\rho_s \Delta x} + b_x \right) \quad (47)$$

358 Computing the modified faced-centered Then, we compute the modified cell
 359 face velocity \mathbf{U}_{FC}^L considering the momentum exchange (see the Appendix:
 360 Momentum exchange with an implicit solve) as follows:

$$\begin{aligned} \mathbf{U}_{f,FC}^L &= \mathbf{U}_{f,FC}^{*\underline{L-}} + \Delta \mathbf{U}_{f,FC} \\ \mathbf{U}_{s,FC}^L &= \mathbf{U}_{s,FC}^{*\underline{L-}} + \Delta \mathbf{U}_{s,FC} \end{aligned} \quad (48)$$

361 Solving the linear equation below is solved to obtain the increment of
 362 velocity with $i,j = 1 : N$ as:

$$\begin{vmatrix} (1 + \beta_{ij}) & -\beta_{ij} \\ -\beta_{ji} & (1 + \beta_{ji}) \end{vmatrix} \begin{vmatrix} \Delta \mathbf{U}_{i,FC} \\ \Delta \mathbf{U}_{j,FC} \end{vmatrix} = \begin{vmatrix} \beta_{ij} (\mathbf{U}_{i,FC}^{*\underline{L-}} - \mathbf{U}_{j,FC}^{*\underline{L-}}) \\ \beta_{ji} (\mathbf{U}_{j,FC}^{*\underline{L-}} - \mathbf{U}_{i,FC}^{*\underline{L-}}) \end{vmatrix}$$

363 Compute faced-centered temperature Compute cell face temperature

364 Similar to the velocity, the faced temperature is computed, for example
 365 in x direction, as:

$$\begin{aligned} \underbrace{T_{fx}^{\underline{nL-}}}_{\text{gathered}} &= \frac{(\bar{\rho}T)_{fx,R}^n + (\bar{\rho}T)_{fx,L}^n}{\bar{\rho}_{fx,L}^n + \bar{\rho}_{fx,R}^n} \\ \underbrace{\frac{T_{fx}}{T_{sx}^{L-}}}_{\text{gathered}} &= \frac{(\bar{\rho}T)_{sx,R}^n + (\bar{\rho}T)_{sx,L}^n}{\bar{\rho}_{sx,L}^n + \bar{\rho}_{sx,R}^n} \end{aligned} \quad (49)$$

366 equation Computing the modified faced-centered Then, we compute the
 367 modified cell face temperature T_{FC}^L considering the energy exchange (see
 368 the Appendix: Momentum and energy exchange with an implicit solver) as
 369 follows:

$$\begin{aligned} T_{f,FC}^L &= T_{f,FC}^{\text{nL}} + \Delta T_{f,FC} \\ T_{s,FC}^L &= T_{s,FC}^{\text{nL}} + \Delta T_{s,FC} \end{aligned} \quad (50)$$

370 Solving the linear equation below to obtain is solved to determine the
 371 increment of velocity with $i,j = 1 : N$ as:

$$\begin{vmatrix} (1 + \eta_{ij}) & -\eta_{ij} \\ -\eta_{ji} & (1 + \eta_{ji}) \end{vmatrix} \begin{vmatrix} \Delta T_{i,FC} \\ \Delta T_{j,FC} \end{vmatrix} = \begin{vmatrix} \eta_{ij}(T_{i,FC}^{\text{nL}} - T_{j,FC}^{\text{nL}}) \\ \eta_{ji}(T_{j,FC}^{\text{nL}} - T_{i,FC}^{\text{nL}}) \end{vmatrix}$$

372 Compute fluid pressure (implicit scheme)

373 For single phase flow, the increment of the fluid pressure can be computed
 374 as:

$$\kappa_f \frac{\Delta P}{dt} = \nabla^c \cdot \mathbf{U}_{f,FC}^{n+1} \quad (51)$$

375 For multi-phase flows, the increment of the fluid pressure of the mixture can
 376 be computed as:

$$\kappa \frac{\Delta P}{dt} = \sum_{f=1}^{N_f} \nabla^c \cdot (\phi_{f,FC} \mathbf{U}_{f,FC})^{n+1} \quad (52)$$

377 where $\kappa = \sum_{f=1}^{N_f} (\phi_{f,FC} \kappa_f) / \sum_{f=1}^{N_f} (\phi_{f,FC})$. Then, the fluid pressure at cell
 378 center is:

$$P_c^{n+1} = P_c^{\text{eqc}} + \Delta P_c^n \quad (53)$$

379 Finally, the faced-centered cell face advanced fluid pressure is:

$$P_{FC}^{n+1} = \left(\frac{P_{c,L}^{n+1}}{\bar{\rho}_{f,L}^n} + \frac{P_{c,R}^{n+1}}{\bar{\rho}_{f,R}^n} \right) / \left(\frac{1}{\bar{\rho}_{f,L}^n} + \frac{1}{\bar{\rho}_{f,R}^n} \right) = \left(\frac{P_{c,L}^{n+1} \bar{\rho}_{f,R}^n + P_{c,R}^{n+1} \bar{\rho}_{f,L}^n}{\bar{\rho}_{f,L}^n \bar{\rho}_{f,R}^n} \right) \quad (54)$$

380 Compute viscous shear stress term of the fluid phase

381 This part compute the viscous shear stress $\Delta(m\mathbf{U})_{fc,\tau} \Delta(m\mathbf{U})_{f,\text{ext}}$ for a
 382 single viscous compressible Newtonian fluid and optionally shear stress
 383 induced by the turbulent model.

384 *Compute nodal internal temperature of the solid phase*

385 The nodal internal temperature rate is computed based on the heat con-
 386 duction model as below:

$$dT_{si}^{L-} = \frac{(\Delta W_{si}^n + \Delta W_{fric,i}^n + \nabla^i \cdot \mathbf{q}_{si}^n)}{m_{si}^n c_v} \quad (55)$$

387 where $\Delta W_{si}^n = \boldsymbol{\sigma}' : \frac{D_s(\boldsymbol{\epsilon}_s^p)}{Dt}$ is the mechanical work rate computed from the
 388 constitutive model with $\boldsymbol{\epsilon}_s^p$ is the plastic strain, $\Delta W_{fric,i}^n$ is the work rate
 389 ~~eompted~~computed from the contact law due to the frictional sliding between
 390 solid materials. The heat flux is $\mathbf{q}_s = \bar{\rho}_s \beta_s \nabla T_s$ with β_s being the thermal
 391 conductivity of the solid materials.

$$T_{si}^{L-} = T_{si}^n + dT_{si}^{L-} \quad (56)$$

392 *Compute and integrate acceleration of the solid phase*

393 After interpolating from material points to the nodes, the nodal acceler-
 394 ~~ation and velocity are ealculate bycalculated by:~~

$$\mathbf{a}_{si}^{L-} = \frac{\mathbf{f}_{si}^{int,n} + \mathbf{f}_{si}^{ext,n}}{m_{si}^n} + \mathbf{g} \quad (57)$$

$$\mathbf{U}_{si}^{L-} = \mathbf{U}_{si}^n + \mathbf{a}_{si}^{L-} \Delta t \quad (58)$$

396 *Compute Lagrangian value (mass, momentum and energy)*

397 For the fluid phase, the linear momentum rate, the energy rate are:~

$$\Delta(m\mathbf{U})_{fc} = V n_c^n \nabla^c P_c^{n+1} + \Delta(m\mathbf{U})_{fc,\tau} + V \bar{\rho}_{fc}^n g \quad (59)$$

$$\Delta(me)_{fc} = V n_c^n P_c^{n+1} \nabla^c \cdot \mathbf{U}_{f,FC}^* + \nabla^c \cdot \mathbf{q}_{fc}^n \quad (60)$$

399 The Lagrangian value of the mass, linear momentum and energy of fluid
 400 phases without momentum exchange are:~

$$m_{fc}^L = V \bar{\rho}_{fc}^n \quad (61)$$

$$(m\mathbf{U})_{fc}^{L-} = V \bar{\rho}_{fc}^n \mathbf{U}_{fc}^n + \Delta(m\mathbf{U})_{fc} \quad (62)$$

$$(me)_{\underline{\text{fc}}\underline{\text{f.c}}}^{L-} = V \bar{\rho}_{\underline{\text{fc}}\underline{\text{f.c}}}^n T_{\underline{\text{fc}}\underline{\text{f.c}}}^n c_v + \Delta(me)_{\underline{\text{fc}}\underline{\text{f.c}}} \quad (63)$$

403 For the solid phase, the Lagrangian value of the linear momentum and energy
404 of solid phase are:

$$m_{sc}^L = m_{sc}^n \quad (64)$$

$$(m\mathbf{U})_{sc}^{L-} = \sum S_{ci} m_{si}^n \mathbf{U}_{si}^{L-} + V(1 - n_c^n) \nabla^c P_{\textcolor{red}{fc}}^{n+1} \quad (65)$$

$$(me)_{sc}^{L-} = \sum_i S_{ci} m_{si}^n T_{si}^L c_v \quad (66)$$

⁴⁰⁷ To consider the momentum exchange, the Lagrangian velocity is modified as:

$$\begin{aligned} \mathbf{U}_{\underline{\mathbf{f}}\underline{\mathbf{c}}\underline{\mathbf{L}}\underline{\mathbf{c}}}^L &= \mathbf{U}_{\underline{\mathbf{f}}\underline{\mathbf{c}}\underline{\mathbf{L}}\underline{\mathbf{c}}}^{L-} + \Delta \mathbf{U}_{\underline{\mathbf{f}}\underline{\mathbf{c}}\underline{\mathbf{L}}\underline{\mathbf{c}}} \\ \mathbf{U}_{sc}^L &= \mathbf{U}_{sc-}^{L-} + \Delta \mathbf{U}_{sc} \end{aligned} \quad (67)$$

where the cell-centered intermediate velocity can be calculated by:

$$U_{\underline{fc}\underline{fc}} = \frac{(mU)_{fc}^{L-}}{m_{fc}^L} \frac{(mU)_{f,c}^{L-}}{\tilde{m}_{f,c}^L} \quad (68)$$

$$U_{sc}^{L-} = \frac{(mU)_{sc}^{L-}}{m_{sc}^L}$$

410 And the increment of the velocity $\underline{U}_{fc} \underline{U}_{lc}$, ΔU_{sc} can be computed by solving
 411 the linear equation with $i,j = 1 : N$ as:

$$\begin{vmatrix} (1 + \beta_{ij}) & -\beta_{ij} \\ -\beta_{ji} & (1 + \beta_{ji}) \end{vmatrix} \begin{vmatrix} \Delta U_{i,c} \\ \Delta U_{j,c} \end{vmatrix} = \begin{vmatrix} \beta_{ij}(U_{i,c}^{*\text{L-}} - U_{j,c}^{*\text{L-}}) \\ \beta_{ji}(U_{j,c}^{*\text{L-}} - U_{i,c}^{*\text{L-}}) \end{vmatrix}$$

412 To consider the energy exchange, the Lagrangian temperature is modified as:

$$T_{\underline{fc}\underline{lc}}^L = T_{\underline{fc}\underline{lc}}^{L-} + \Delta T_{\underline{fc}\underline{lc}} \quad (69)$$

$$T_{sc}^L = T_{sc}^{L-} + \Delta T_{sc}$$

where the cell-centered intermediate temperature can be calculated by:

$$T_{\frac{fc}{fc, c}}^{L-} = \frac{(mT)_{fc}^{L-}}{m_{fc}^L c_v} \frac{(mT)_{f,c}^{L-}}{\underbrace{m_{f,c}^L c_v}_{(70)}}$$

415 And the increment of the velocity can be computed by solving the linear
 416 equation with $i,j = 1 : N$ as:

$$\begin{vmatrix} (1 + \eta_{ij}) & -\eta_{ij} \\ -\eta_{ji} & (1 + \eta_{ji}) \end{vmatrix} \begin{vmatrix} \Delta T_{i,c} \\ \Delta T_{j,c} \end{vmatrix} = \begin{vmatrix} \eta_{ij}(T_{i,c}^{\text{nL}} - T_{j,c}^{\text{nL}}) \\ \eta_{ji}(T_{j,c}^{\text{nL}} - T_{i,c}^{\text{nL}}) \end{vmatrix}$$

417 Finally, we obtain the cell-centered solid acceleration and temperature rate
 418 as: $\ddot{\cdot}$

$$d\mathbf{U}_{sc}^L = \frac{(m\mathbf{U})_{sc}^L - (m\mathbf{U})_{sc}^n}{m_{sc}^L \Delta t} \quad (71)$$

$$dT_{sc}^L = \frac{(me)_{sc}^L - (me)_{sc}^n}{m_{sc}^L c_v \Delta t} \quad (72)$$

420 *Compute Lagrangian specific volume of the fluid phase*

421 To compute the Lagrangian value of the specific volume of the fluid phase,
 422 we need to compute the Lagrangian temperature rate as below: $\dot{\cdot}$

$$T_{fc}^{n+1} = \frac{(me)_{fc}^L}{m_{fc}^L c_v} \frac{(me)_{f,c}^L}{\tilde{m}_{f,c}^L c_v} \quad (73)$$

$$\frac{D_f T_{fc}}{Dt} \frac{D_f T_{f,c}}{Dt} = \frac{T_{fc}^{n+1} - T_{fc}^n}{\Delta t} \frac{T_{f,c}^{n+1} - T_{f,c}^n}{\Delta t} \quad (74)$$

424 As such, the Lagrangian specific volume rate is:

$$\Delta(mv)_{fc}^{\phi} = V f_{fc}^{\phi} \nabla \cdot \mathbf{U} + (\phi_{fc} \alpha_{fc} \frac{D_f T_{fc}}{Dt} \frac{D_f T_{f,c}}{Dt} - f_{fc}^{\phi} \sum_{n=1}^N \phi_{nc} \alpha_{nc} \frac{D_n T_{nc}}{Dt} \frac{D_n T_{n,c}}{Dt}) \quad (75)$$

425 where $f_f^{\phi} = (\phi_f \kappa_f) / (\sum_{n=1}^N \phi_n \kappa_n)$ and $\mathbf{U} = \nabla \cdot (\sum_{s=1}^{N_s} \phi_{sc} \mathbf{U}_{sc} + \sum_{f=1}^{N_f} \phi_{fc} \mathbf{U}_{fc})$
 426 Finally, the Lagrangian specific volume is: $\ddot{\cdot}$

$$(mv)_{fc}^L = V \bar{\rho}_{f,c}^n v_{fc}^n + \Delta(mv)_{fc}^{\phi} \quad (76)$$

427 *Compute advection term and advance in time*

428 The time advanced mass, linear momentum, energy and specific volume
429 are:

$$430 \quad m_{\underline{fc}\underline{f},c}^{n+1} = m_{\underline{fc}\underline{f},c}^L - \Delta t \nabla \cdot (\bar{\rho}_{\underline{fc}\underline{f},c}^L, \mathbf{U}_{f,FC}^L) \quad (77)$$

$$431 \quad (m\mathbf{U})_{\underline{fc}\underline{f},c}^{n+1} = (m\mathbf{U})_{\underline{fc}\underline{f},c}^L - \Delta t \nabla \cdot ((\bar{\rho}\mathbf{U})_{\underline{fc}\underline{f},c}^L, \mathbf{U}_{f,FC}^L) \quad (78)$$

$$432 \quad (me)_{\underline{fc}\underline{f},c}^{n+1} = (me)_{\underline{fc}\underline{f},c}^L - \Delta t \nabla \cdot ((\bar{\rho}c_v T)_{\underline{fc}\underline{f},c}^L, \mathbf{U}_{f,FC}^L) \quad (79)$$

$$433 \quad (mv)_{\underline{fc}\underline{f},c}^{n+1} = (mv)_{\underline{fc}\underline{f},c}^L - \Delta t \nabla \cdot ((\bar{\rho}v)_{\underline{fc}\underline{f},c}^L, \mathbf{U}_{f,FC}^L) \quad (80)$$

434 Finally, the state variables of the fluid phases of the next time step are:~

$$435 \quad \bar{\rho}_{\underline{fc}\underline{f},c}^{n+1} = \frac{m_{fc}^{n+1}}{\underline{V}} \frac{m_{f,c}^{n+1}}{\underline{V}} \quad (81)$$

$$436 \quad \mathbf{U}_{\underline{fc}\underline{f},c}^{n+1} = \frac{(m\mathbf{U})_{fc}^{n+1}}{\underline{m_{fc}^{n+1}}} \frac{(m\mathbf{U})_{f,c}^{n+1}}{\underline{m_{f,c}^{n+1}}} \quad (82)$$

$$437 \quad T_{\underline{fc}\underline{f},c}^{n+1} = \frac{(me)_{fc}^{n+1}}{\underline{m_{fc}^{n+1}}} \frac{(me)_{f,c}^{n+1}}{\underline{m_{f,c}^{n+1}}} \quad (83)$$

$$438 \quad v_{\underline{fc}\underline{f},c}^{n+1} = \frac{(mv)_{fc}^{n+1}}{\underline{m_{fc}^{n+1}}} \frac{(mv)_{f,c}^{n+1}}{\underline{m_{f,c}^{n+1}}} \quad (84)$$

439 *Interpolate from cell to node of the solid phase*

440 First we interpolate the acceleration, velocity and temperature rate to
441 the node as below:

$$442 \quad \mathbf{a}_{si}^n = \sum S_{ci} d\mathbf{U}_{sc}^L \quad (85)$$

$$443 \quad \mathbf{U}_{si}^{n+1} = \sum S_{ci} d\mathbf{U}_{sc}^L \Delta t \quad (86)$$

$$444 \quad dT_{si}^n = \sum S_{ci} dT_{sc}^L \quad (87)$$

445 Then the boundary condition and contact forces f_{si}^{fric} are applied to the nodal
446 velocity and the acceleration is modified by:~

$$447 \quad \mathbf{a}_{si}^n = \frac{\mathbf{v}_{si}^{n+1} - \mathbf{v}_{si}^n}{\Delta t} \quad (88)$$

444 *Update the particle variables*

445 The state variables of the solid phase [$\mathbf{U}_{sp}^{n+1}, \mathbf{x}_{sp}^{n+1}, \nabla \mathbf{U}_{sp}^{n+1}, T_{sp}^{n+1}, \nabla T_{sp}^{n+1}, \mathbf{F}_{sp}^{n+1}, V_{sp}^{n+1}$]
 446 (velocity, position, velocity gradient, temperature, temperature gradient, de-
 447 formation gradient, volume) are updated [here](#) as:

$$\mathbf{U}_{sp}^{n+1} = \mathbf{U}_{sp}^n + \sum S_{sp} \mathbf{a}_{si}^n \Delta t \quad (89)$$

$$\mathbf{x}_{sp}^{n+1} = \mathbf{x}_{sp}^n + \sum S_{sp} \mathbf{U}_{si}^{n+1} \Delta t \quad (90)$$

$$\nabla \mathbf{U}_{sp}^{n+1} = \sum \nabla S_{sp} \mathbf{U}_{si}^{n+1} \quad (91)$$

$$T_{sp}^{n+1} = T_{sp}^n + \sum S_{sp} dT_{si}^n \Delta t \quad (92)$$

$$\nabla T_{sp}^{n+1} = \sum \nabla S_{sp} T_{sp}^n \Delta t \quad (93)$$

$$\mathbf{F}_{sp}^{n+1} = (\mathbf{I} + \nabla \mathbf{U}_{sp}^{n+1} \Delta t) \mathbf{F}_{sp}^n \quad (94)$$

$$V_{sp}^{n+1} = \det(\mathbf{F}_{sp}^{n+1}) V_{sp}^o \quad (95)$$

454 Finally, the effective stress $(\sigma')^{n+1}$ is updated from the constitutive model
 455 and the pore water pressure is interpolated from the cell as:

$$p_f^{n+1} = \sum S_{si} P_c^{n+1} \quad (96)$$

456 Numerical examples

457 All input files and the analytical calculations in this section are provided
 458 in the Github repository (https://github.com/QuocAnh90/Uintah_NNTU)
 459 for the reproduction of the numerical results.

460 To prevent repetition, we present the parameters of water and air, which
 461 remain consistent across all simulations. The water has a bulk modulus of 2
 462 GPa, a density of 998 kg/m³ at a reference temperature of 5 degrees Celsius
 463 and a reference pressure of 10325 Pa (1atm), a dynamic viscosity μ_f of 1
 464 mPa s). The air has a ideal gas with a density of 1.17 kg/m³ at a reference
 465 temperature of 5 degrees Celsius and a reference pressure of 10325 Pa (1atm),
 466 a dynamic viscosity μ_f of $18.45E^{-3}$ mPa s).

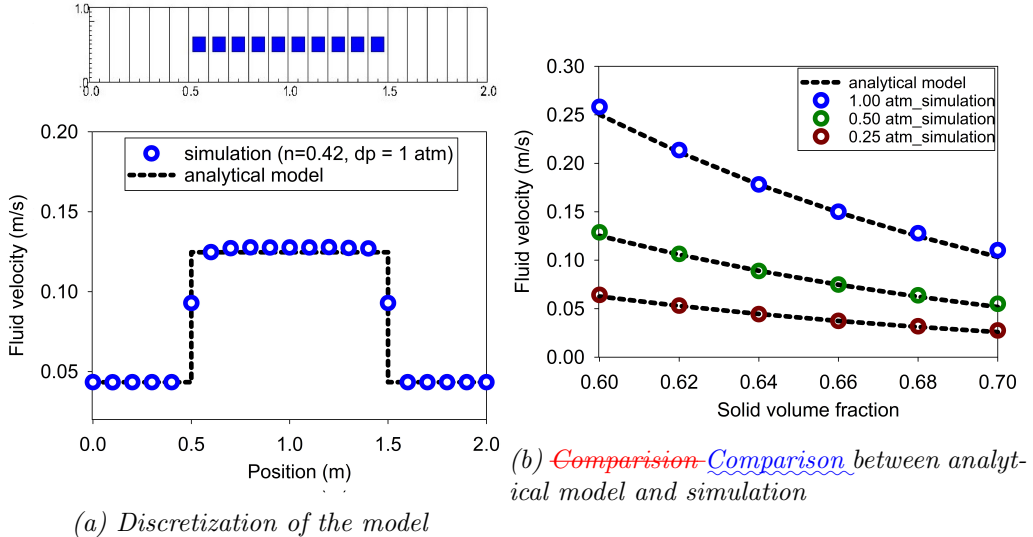


Figure 7: Numerical results of the fluid flow through isothermal porous media

467 Fluid Flow through isothermal porous media

468 Fluid flow through porous media is important in many engineering disciplines,
 469 like predicting water flow in soil. Fluid flow velocity in one dimension
 470 can be calculated from the porous media's hydraulic conductivity K as:

$$471 \quad U_f = K \frac{\Delta p_f}{L} \quad (97)$$

472 If the Carman-Kozeny formula is adopted $F = 10\phi_s/(1 - \phi_s)^2$, the hydraulic
 473 conductivity will be expressed as $K = d^2(1 - \phi_s)^3 / 180\mu\phi_s^2$. Then, the analytical formula of average velocity in one dimension through
 474 the porous media is:
 475

$$476 \quad U_f = \frac{1}{n} \frac{d^2(1 - \phi_s)^3}{180\mu\phi_s^2} \frac{D_p^2(1 - \phi_s)^3}{180\phi_s^2\mu_f} \frac{\Delta p_f}{L} \quad (98)$$

477 Our numerical model is validated by modeling fluid flow through a 1m
 478 long porous media. This fluid has water properties (bulk modulus is 2GPa,
 479 density is 998 kg/m³ at 5 degrees Celsius and 10325 Pa (1atm) pressure,
 480 dynamic viscosity μ is 1mPa s). The porous media is modeled by elastic
 481 material with Young's modulus is 10 MPa, Poisson's ratio is 0.3, and density
 482 is 2650 kg/m³. The volume fraction of porous media ϕ_s is [0.6, 0.62, 0.66,

483 0.68, 0.7] and the average grain diameter d is 1mm. The model is discretized
 484 in 20 finite element and the porous media in 10 finite element with 1 material
 485 point per element. The pressure gradient is applied with three different value
 486 [0.25, 0.5, 1] atm. Figure 7 shows a good agreement of fluid flow prediction
 487 between the theory and the model.

488 *Isothermal consolidation*

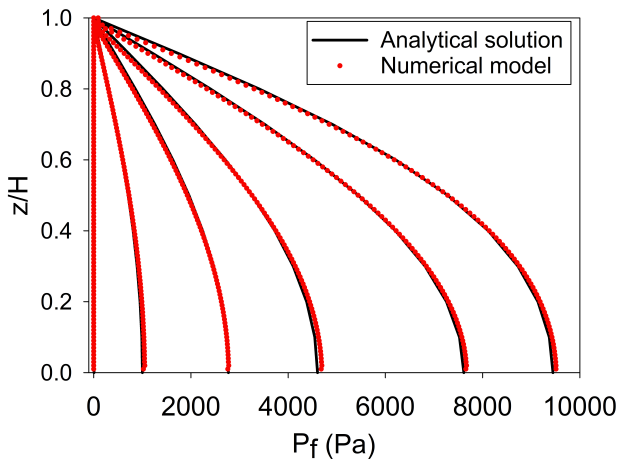


Figure 8: Comparison between analytical solution and numerical solution

489 A common benchmark ~~for~~ for a fully saturated porous ~~meida~~~~media~~ is
 490 the simulation of one-dimensional consolidation. Using the Carman-Kozeny
 491 formula, the time-dependent pressure can be ~~evaluated~~~~calculated~~ as:

$$p_f = \sum_{m=1}^{\infty} \frac{2F_{ext}}{M} \sin\left(\frac{Mz}{H}\right) e^{-M^2 T_v} \text{ with } M = \frac{\pi}{2}(2m + 1) \quad (99)$$

492 where the consolidation rate $T_v = C_v t / H^2$, the consolidation coefficient $C_v =$
 493 $E_v n^3 d^2 / (180(1 - n)^2 \mu)$ and the Oedometer modulus $E_v = E(1 - v) / (1 +$
 494 $v) / (1 - 2v)$. Our numerical model is validated by modeling the consolidation
 495 of a 1m column. ~~This fluid has water properties (bulk modulus is 2GPa,~~
 496 ~~density is 998 kg/m3 at 5 degrees Celsius and 101325 Pa (1atm) pressure,~~
 497 ~~dynamic viscosity μ is 1mPa s).~~ The porous media is modeled by elastic
 498 material with Young's modulus is 10 MPa, Poisson's ratio is 0.3, and density
 499 is 2650 kg/m3. The volume fraction of porous media ϕ_s is 0.7 which is

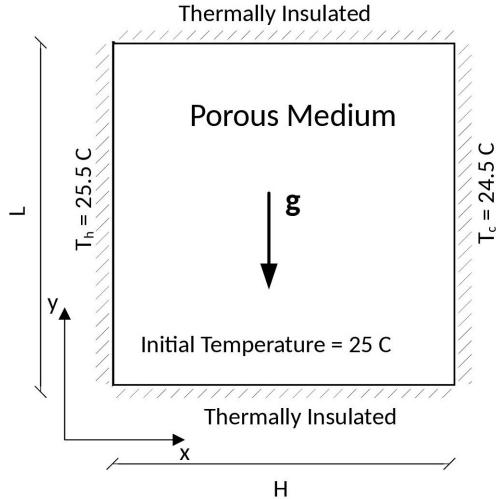


Figure 9: Model schematic [23]

equivalent to the porosity of 0.3 and the average grain diameter d is 1mm.
 The model is discretized in 100 finite element with 1 material point per element. The external pressure applies to the top of the column is 10 kPa. Figure 8 shows a good agreement of fluid flow prediction between the theory and the model.

505 Thermal induced cavity flow

Another ~~benchmark~~ is the thermal induced cavity flow in porous media. Temperature and velocity distributions are calculated for a square non-deformable saturated porous media. The top and bottom walls are insulated, and the left and right walls are at fixed ~~temperatures differing by temperature gradient of~~ 1 degree. The fluid motion at steady state are cavity flow due to the temperature induced density variation. The numerical is validated by comparing with the numerical solution of the finite element method. The ~~fluid has water properties (bulk modulus is 2GPa, density is 998 kg/m³ at 5 degrees Celsius and 10325 Pa (1atm) pressure, dynamic viscosity μ is 1 mPa s)~~. The porous media is modeled by non deformable material, and density is 2500 kg/m³. The specific heat capacity of the water and porous skeleton are 4181 J/kg.K and 835 J/kg.K respectively. The thermal conductivity of the water and porous skeleton are 0.598 W/m.K and 0.4 W/m.K. The volume fraction of porous media ϕ_s is 0.6 which is equivalent

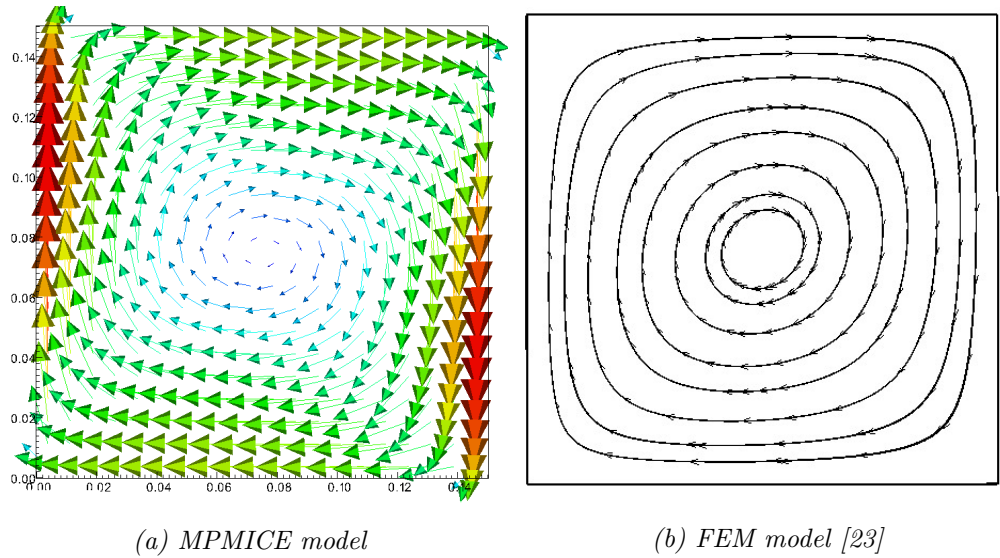


Figure 10: Comparison between MPMICE model and FEM model

to the porosity of 0.4 and the average grain diameter d is 1mm. The model is discretized in 20×20 finite element with 4 material point per element. Figure 10 shows a good agreement of numerical results of the model compared with the numerical solution of the finite element method.

Underwater debris flow

The numerical example is validated by using the experimental work of Rzadkiewicz et al. 's experiment on submarine debris flow [24]. During theIn their experiment, sand in-within a triangular box is released and then slides along a rigid bed inclined at 45 degrees under water -(see Figure 11-0.4 seconds subfigure0.8 seconds subfigureSimulation of underwater debris flow figureMaterials Bulk modul(Pa)tabular Shear modul(Pa)tabular Density(kg/m³)tabular Temp(C)tabular Dynamic viscosity(Pa·s)tabular Yield stress(Pa)tabular Water(at surface)tabular2.15e9-999.85855e-6-Air(at top boundary)tabular-1.177518.45e-6-Sand(porous media)tabular8.33e620e61985.5-200-Rigid bed(solid)tabular117e743.8e78900.5--tabularNumerical parameters for the underwater submarine debris tableIn-). The material properties in the numerical model , the material properties are selected based on the experiment by Rzadkiewicz et al[24]. Sand has . [24]. The sand is characterized by a saturated density of 1985 kg/m³ and yield stress of 200 Pa. a friction angle

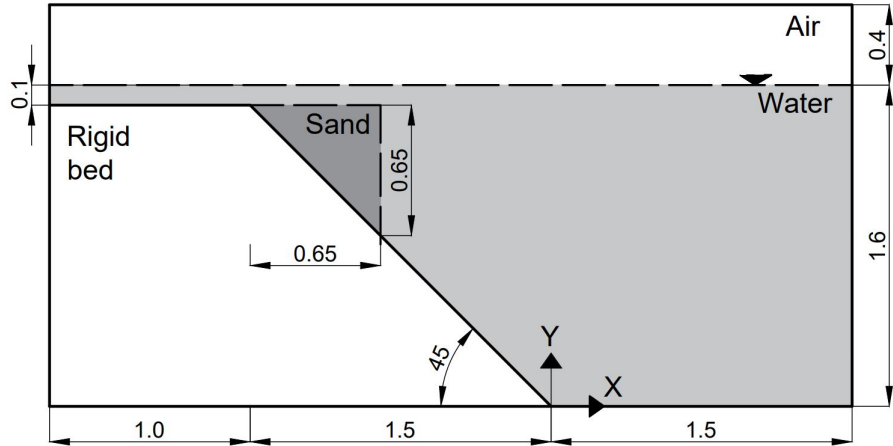


Figure 11: Model schematic

539 of 10 degrees. The effect of Young's modulus has little effect on debris flow
 540 run-out because of the extreme large is negligible due to the extreme deformation of the debris. Therefore, we select 50 MPa, so a Young's modulus
 541 with 0.25 of 50 MPa with a Poisson's ratio of 0.25 is chosen. The rigid bed is
 542 much stiffer with being much stiffer, has bulk modulus and shear modulus
 543 values of $117E^7$ Pa and $43.8E^7$ Pa. Under gravity, the density of the water
 544 at the surface is 999.8 kg/m^3 at the pressure of 1 atm. At the top boundary,
 545 the air has a density of 1.17 kg/m^3 at the atmospheric pressure of 1 atm.
 546 At 5 Celsius degrees, air and water have viscosity of $18.45E^{-3}$ mPa s and
 547 1 mPa s , respectively. The numerical parameters used in this example are
 548 presented in Table 1.

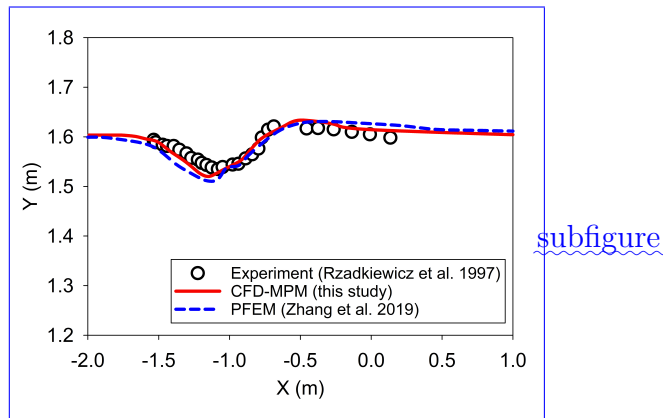
549 On The boundary conditions imposed in the numerical model are as follows:
 550 on all boundary faces, the Dirichlet boundary condition is imposed for velocity
 551 (u velocity is set to zero ($U = 0 \text{ m/s}$) and temperature the temperature is
 552 set to 5 degrees Celsius ($T = 5 \text{ Celsius degrees}$), while the Neuman boundary
 553 condition is imposed at the top boundary for pressure ($^\circ\text{C}$). At the top boundary,
 554 the pressure has a Neumann boundary condition of $dp/dx = 0 \text{ kPa}$) and
 555 density (, and the density has a Neumann boundary condition of $d\rho/dx =$
 556 0 kg/m^3). For the background mesh , there are . The background mesh
 557 consists of $700 \times 400 = 280,000$ cells. In each cell of cells, resulting in a total
 558 of 280,000 cells. Each cell in the debris flow and rigid bed , there are contains
 559 2 x 2 material points.

560 0.4 seconds subfigure0.8 seconds subfigureSimulation of underwater debris

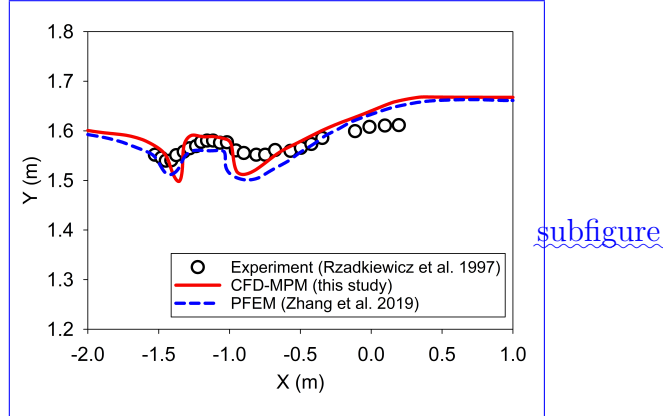
562 flow figureFigure ?? and ?? show Figure 13b illustrates snapshots of the
563 underwater debris flow sliding in the plane at 0.4 s and 0.8 s. Our simulations
564 match the computed results from Rzadkiewicz et al. [24]. The model also
565 captures, demonstrating that the model captures the typical hydroplaning
566 mechanism of the underwater debris flow(hydroplaning means the debris
567 flow is lifted up and no longer in . Hydroplaning refers to the lifting of the
568 debris flow, causing it to lose contact with the bottom layer). The elevation
569 of the free surface at 0.4s and 0.8s is compared between our proposed
570 method and other methods in Figure 12. Once again, our computed results
571 were consistent with both the experiment and others computational Our
572 computed results align well with the experimental results [7].
573 Unlike other computational models based that rely on total stress analysis
574 , the proposed model based on the [5, 6, 7, 8], our proposed model utilizes
575 effective stress analysiswhich allows to analyze the , enabling the analysis
576 of water pressure and temperature in within the debris flow. saturated
577 debris flow using MPM subfigureunderwater debris flow using MPMICE
578 subfigureSimulation of underwater debris flow figureWe also explore the difference
579 Additionally, we investigate the differences between underwater debris flow
580 and saturated debris flow in terms of interacting with obstacletheir interaction
581 with obstacles. Figure 13 shows the snapshot of the simulations of presents
582 snapshots of simulations of both underwater and saturated debris flow. The
583 saturated debris flow (see Figure 13a) behaves like frictional flowas grain
584 exhibits behavior similar to frictional flow, where grains have contact forces
585 with each other. On the other handConversely, the underwater debris flow
586 (see Figure 13b) behaves like turbulent flowas grains are turbulent flow, with
587 grains being separated from each other and exhibit exhibiting no contact
588 forces between grains. (as reflected by the near-zero effective stress in the
589 turbulence domain).

Materials	Bulk modul (Pa)	Shear modul (Pa)	Density (kg/m ³)	Temp (C)	Dynamic viscosity (Pa s)	Friction angle (degrees)
Water (at surface)	2.15e9	-	999.8	5	855e-6	-
Air (at top boundary)	-	-	1.177	5	18.45e-6	-
Sand (porous media)	8.33e6	20e6	1985	5	-	10
Rigid bed (solid)	117e7	43.8e7	8900	5	-	-

Table 1: Numerical parameters for the underwater submarine debris



(a) 0.4 seconds



(b) 0.8 seconds

Figure 12: Evolution of water level in the simulation of underwater debris flow

590 figure figure

591 Validation of soil response to the seismic loading

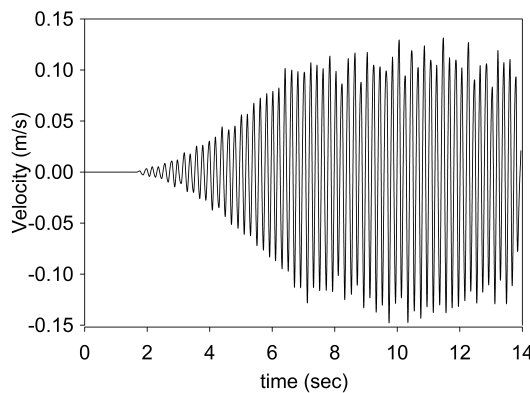


Figure 14: Seismic loading

592 figure

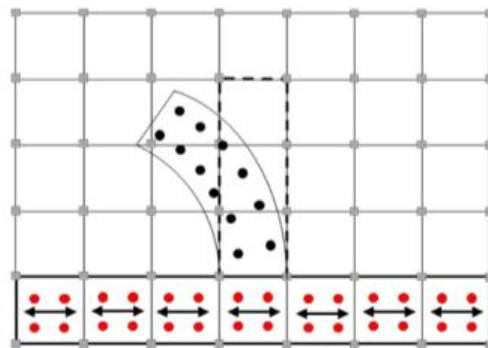
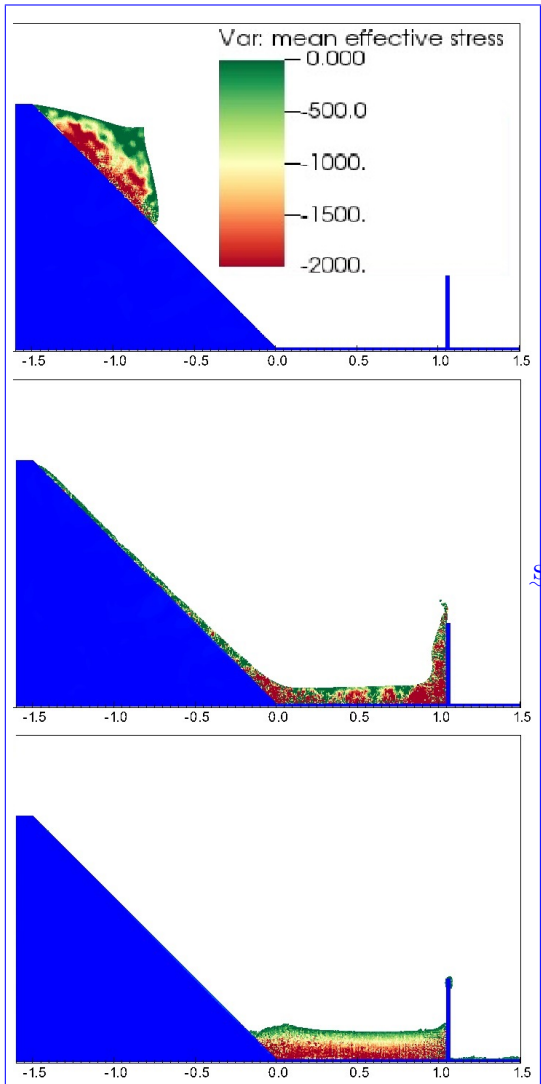


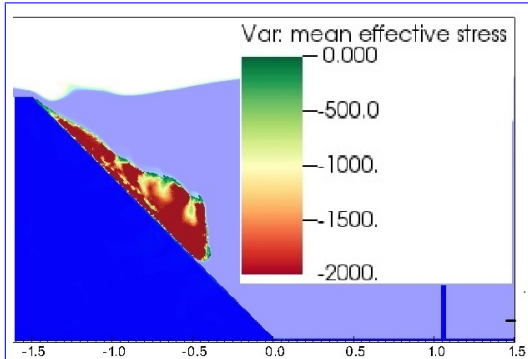
Figure 15: Material points prescribed velocity as kinematic boundary condition [25]

593 figure An experimental study conducted by Hiraoka et al. [26] aimed to
594 investigate the influence of seismic shaking on the deformation of a 0.5 m-high
595 sand slope. The sand used in the experiment was partially saturated, with a
596 moisture content of 10 percent. The provided soil parameters for the Mohr
597 Coulomb model include the effective friction angle of 23 degrees, apparent
598 cohesion of 0.78 kPa, Young's modulus of 2.57 MPa, and Poisson's ratio of



subfigure

(a) *saturated debris flow using MPM*



36

subfigure

599 0.33, and moist unit weight of 16.5 kN/m³. The soil's dilatancy angle was
 600 assumed to be 0 [26]. The experimental setup consisted of a shaking table
 601 box with a steel horizontal base and smooth glass vertical sidewalls. Laser
 602 sensors were used to monitor the displacement of the slope's toe and crest.
 603 Figure 14 displays the velocity-time history employed in the experiment.

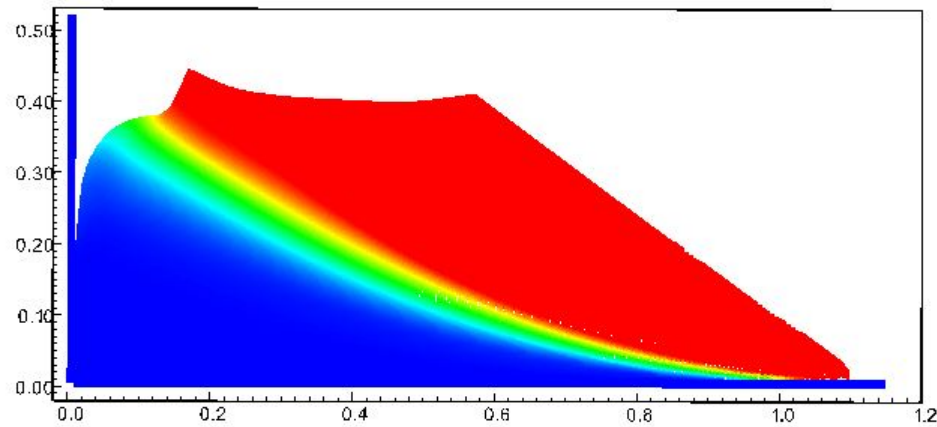


Figure 16: Numerical model of the seismic-induced slope failure with displacement color

604 figure
 605 To simulate the seismic loading in our numerical model, we adopted a
 606 method presented by Alsardi et al. [25], which involves specifying the velocity
 607 at the corresponding material points representing either the shaking table or
 608 the bedrock at the site (see Figure 15). In our simulation, we considered the
 609 horizontal base to be fully rough and the vertical contact to be fully smooth.
 610 The initial stress condition was initiated using gravity and seismic loading
 611 induced the slope failure (see Figure 16).

612 Previous studies by Bhandari et al. [27], Alsardi et al. [25], and Hiraoka et
 613 al. [26] attempted to model this experiment using MPM and SPH models. In
 614 this study, we compared our results with those obtained from other particle-based
 615 methods (Figure 17). The main difference is that we did not apply 5 percent
 616 numerical damping in our model, unlike the other methods. We found
 617 that the final displacement of the slope toe in our MPM model was higher
 618 than that observed in the experiment. Nevertheless, the validation of the
 619 Mohr-Coulomb model under seismic response demonstrated a reasonable soil
 620 behavior in terms of displacement.

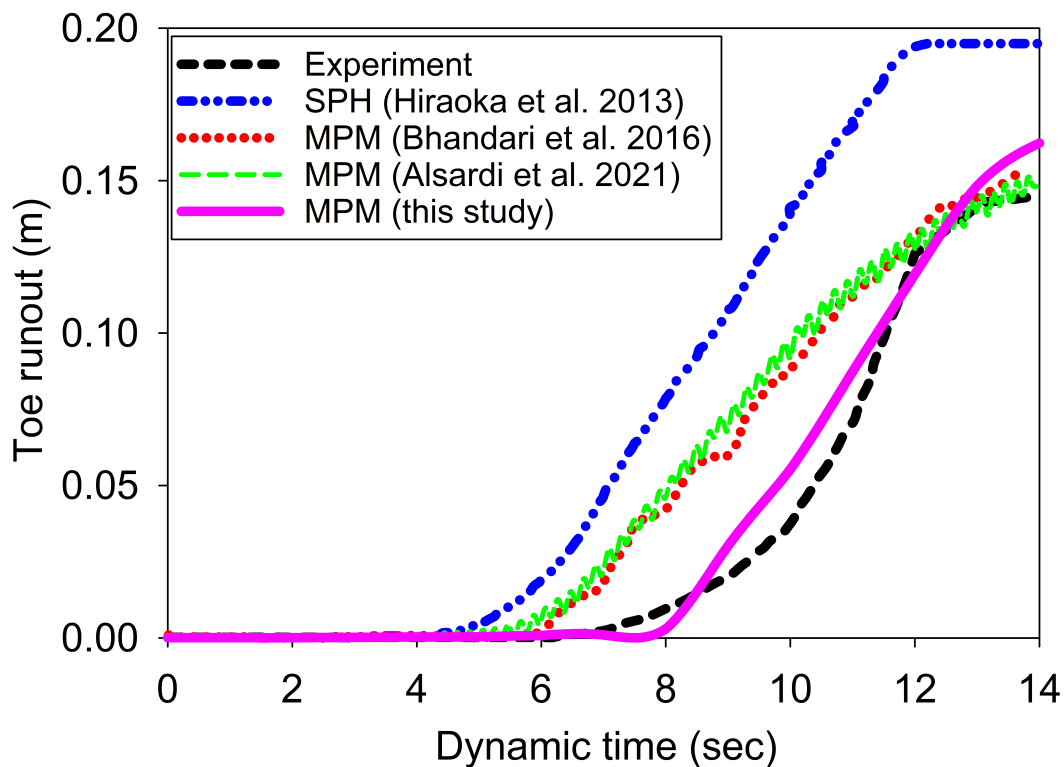


Figure 17: Displacement of the toe of the slope

621 [figure](#)

622 [Earthquake-induced submarine landslides](#)

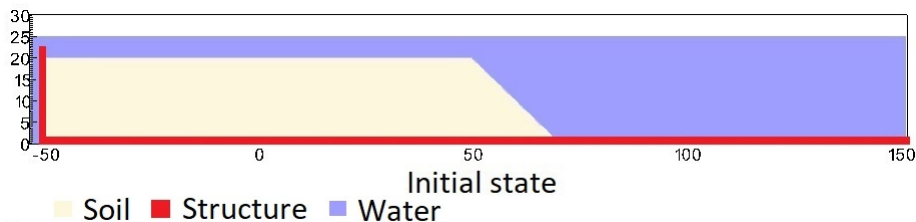


Figure 18: Numerical model simulation of the earthquake-induced submarine land-slide

623 [figure](#)

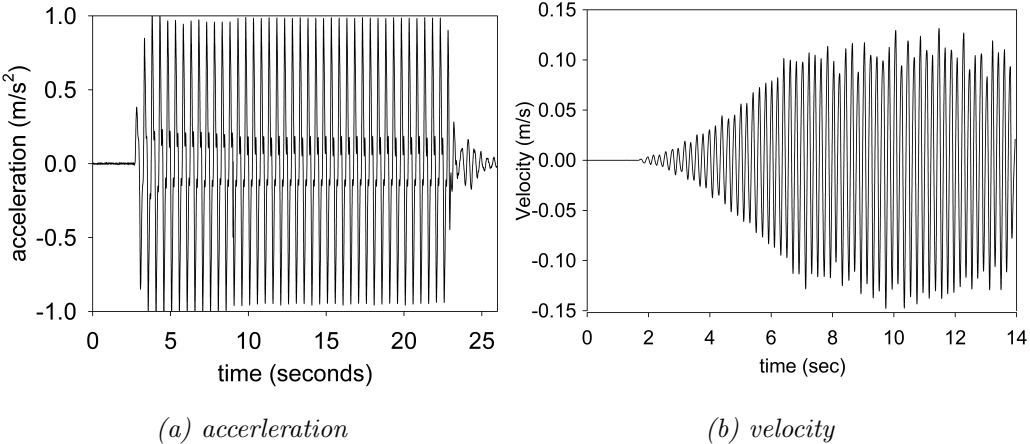


Figure 19: Ground acceleration profile, frequency of 2Hz and magnitude of 1g

In the final example, we perform numerical analysis of the earthquake induced submarine landslides. A plane strain model with the slope under water is shown in Figure 18. A 20m high slope with slope gradient of 45 degrees is placed in a horizontal and vertical structure which was used to be a shaking table to apply earthquake loading. We simplify the earthquake loading by simulating the ground shaking for 20 seconds with the peak constant ground acceleration of 1g and the a constant frequency of 2Hz (Figure 19a). The ground motion is applied in terms of velocity (Figure 19b). The An earthquake of this magnitude can occurred typically for the earthquake of magnitude of more than 6. is possible. For instance, in the case of the 2023 Turkey-Syria Earthquake, significant ground shaking with peak ground acceleration exceeding 1g was observed at numerous locations. This serves as an example of the practical occurrence of such high levels of ground acceleration during seismic events. To generate the seismic loading, the same method was used as presented in the previous numerical example.

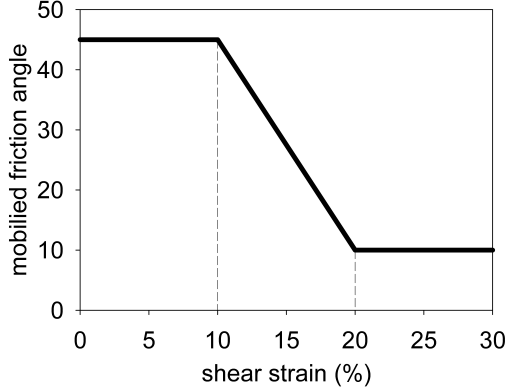


Figure 20: Mobilized friction angle in Mohr Coulomb model

639 A non-associated Mohr-Coulomb model is used for the soil. The soil grain
 640 has the density of 2650 kg/m^3 , Young's modulus of 10 kPa and Poisson's
 641 ratio of 0.3 and zero cohesion. The mobilized friction angle ϕ'_m is governed
 642 following the softening curve (see Figure 20) with the peak friction angle ϕ'_p
 643 of 45 degrees and the residual friction angle ϕ'_r of 10 degrees. The porosity
 644 is 0.3 and the average grain size of the soil is around $0.1 \mu\text{m}$ to mimic the
 645 undrained behavior. The mobilized dilatancy angle is calculated from the
 646 ~~Rowe-stress dilatancy~~ [Rowe's stress dilatancy theory \[28\]](#) as follow:

$$\sin \psi'_m = \frac{\sin \phi'_m - \sin \phi'_r}{1 - (\sin \phi'_r \sin \phi'_m)} \quad (100)$$

647 The solid plane is modeled as a rigid body acted as a shaking table. The con-
 648 tact between horizontal plane and the sand is the frictional contact with the
 649 friction coefficient of 0.1. No artificial damping is applied in the simulation.
 650 The contact between vertical plane and the sand is ~~eonsdered~~ [considered](#) to
 651 be smooth with zero friction coefficient. ~~Under gravity, the density of the~~
~~652 water at the surface is 999.8 kg/m^3 at the pressure of 1 atm. At the top~~
~~653 boundary, the air has a density of 1.17 kg/m^3 at the atmospheric pressure~~
~~654 of 1 atm. At 5 Celcius degrees, air and water have viscosity of $18.45e^{-3} \text{ mPa}$~~
~~655 s and 1 mPa s respectively.~~ On all boundary faces, the symmetric bound-
 656 ary condition is imposed, while the ~~Neuman~~ [Neumann](#) boundary condition
 657 is imposed at the top ~~boundaryfor~~ [boundary for](#) pressure ($d\rho/dx = 0 \text{ kPa}$)
 658 and density ($d\rho/dx = 0 \text{ kg/m}^3$). [Symmetric boundary condition refers to](#)
~~a condition where the normal component of the velocity at the boundary~~

660 face is set to zero, and the tangential component is equal to the tangential
 661 component of the neighboring cells. The mesh size is 0.25×0.25 m with 300852
 662 element cells and 142316 material points. The simulation takes a couple of
 663 hours to perform 60 seconds of the simulation using 4096 CPUs.

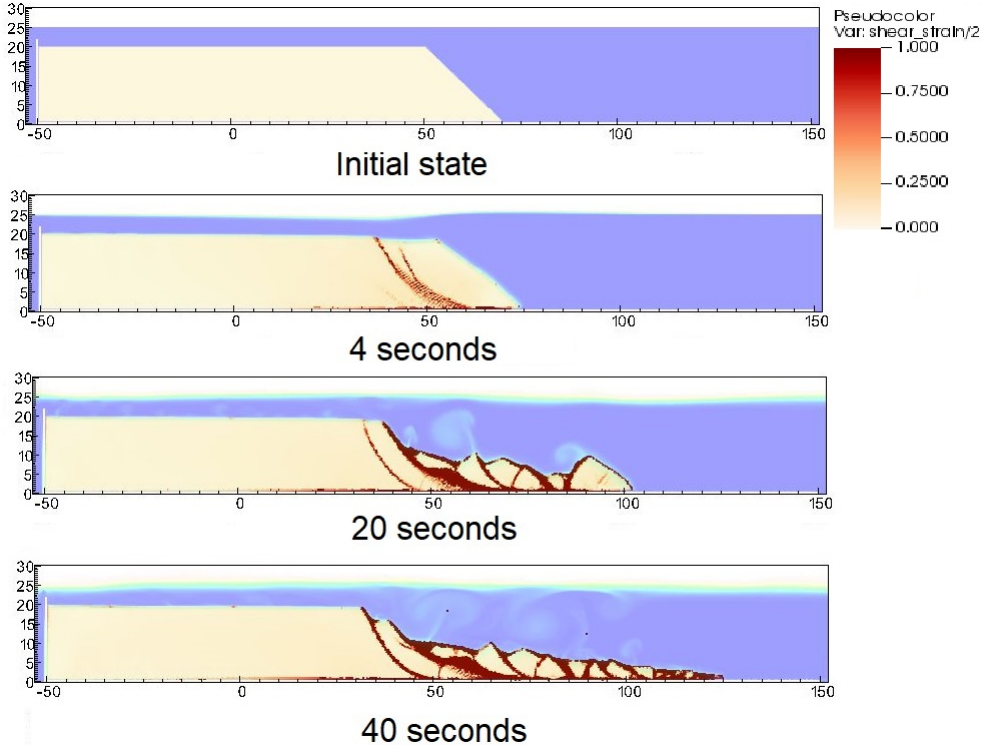


Figure 21: Shear strain during the earthquake-induced submarine landslides

664 We demonstrate the entire process and the mechanism of the earthquake-
 665 induced submarine landslides by showing the shear strain (Figure 21), the
 666 pore water pressure in atm (Figure 22) and the velocity (Figure 23).
 667 The failure mechanism can be characterized as the progressive
 668 failure mechanism. Here are some numerical observation:

- 669 1. At the initial of the seismic event, the seismic loading triggers the
 670 first slide at 3 seconds. At 4 seconds, the debris start to move with the
 671 maximum speed of around 2-3 m/s with multiple shear band developed
 672 in the slope. The wave generated from the submarine slide is around
 673 2-3m towards the slide direction.

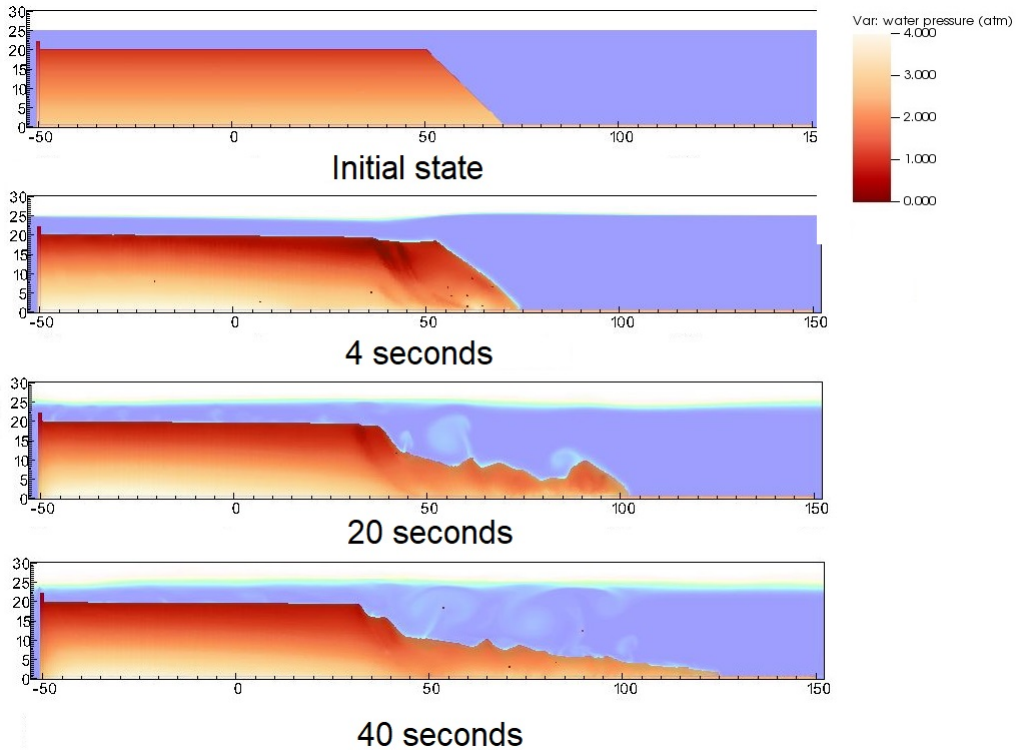


Figure 22: pore water pressure during the earthquake-induced submarine landslides

- 674 2. When the onset of the shear band occurs in the slope (for example
 675 at 4 seconds and 20 seconds), the negative excess pore water pressure
 676 is developed along this shear band with pore water pressure is under
 677 1atm. This is a typical dilatancy behavior when the soil is sheared
 678 rapidly in the undrained behavior.
- 679 3. When the seismic loading ends at 23 seconds, the last shear band is
 680 mobilized and the slope soon reaches to the final deposition. No more
 681 progressive failure developed in the slope. The turbulent flow developed
 682 as the interaction between debris flow and seawater.
- 683 Overall, we show the completed process of the earthquake-induced submarine
 684 landslides involving (1) earthquake triggering mechanism, (2) the onset of the
 685 shear band with the ~~development~~ development of negative excess pore water
 686 pressure, (3) progressive failure mechanism, (4) submarine landslide induced
 687 wave to final deposition.

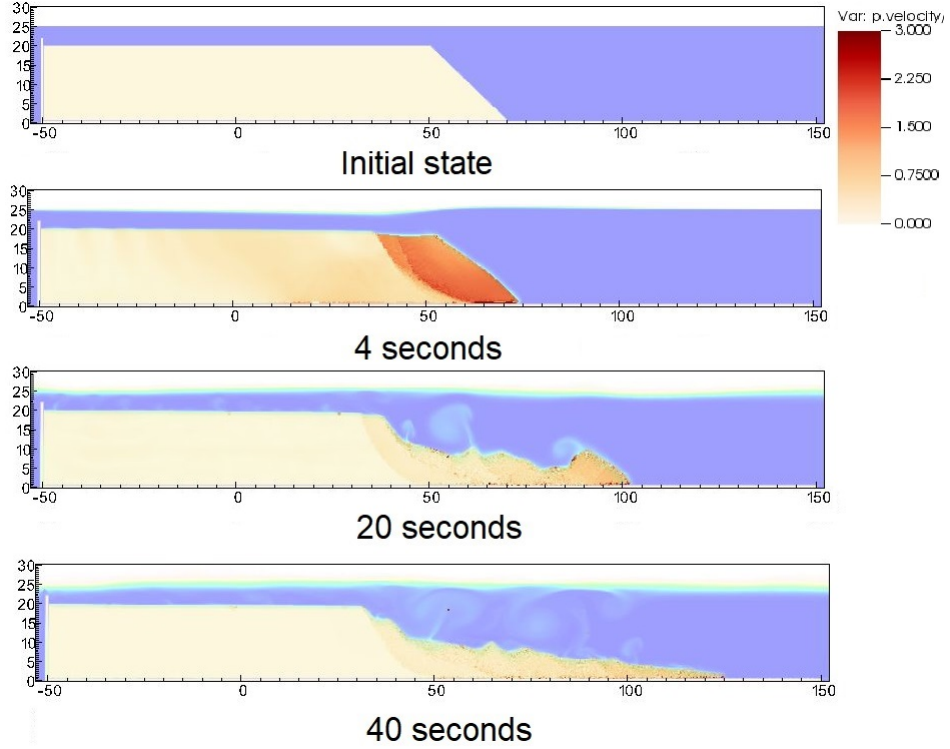


Figure 23: Velocity during the earthquake-induced submarine landslides

688 **Conclusions**

689 We have presented a numerical approach MPMICE for the simulation
 690 of large deformation soil-fluid-structure interaction, emphasizing the simu-
 691 lation of the earthquake-induced submarine landslides. The model uses (1)
 692 the Material Point Method for capturing the large deformation of iso-thermal
 693 porous media and solid structures and (2) Implicit Continuous Eulerian (com-
 694 pressible, conservative multi-material CFD formulation) for modeling the
 695 complex fluid flow including turbulence. This model is implemented in the
 696 high-performance Uintah computational framework and validated against an-
 697 alytical solution and experiment. We then demonstrate the capability of the
 698 model to simulate the entire process of the earthquake induced submarine
 699 landslides.

700 **Acknowledgements**

701 The authors gratefully acknowledge Dr. James Guilkey and Dr. Todd
 702 Harman from the University of Utah for sharing the insight on the theoretical
 703 framework of MPMICE which this work is based. This project has received
 704 funding from the European Union's Horizon 2020 research and innovation
 705 program under the Marie Skłodowska-Curie Actions (MSCA) Individual Fel-
 706 lowship (Project SUBSLIDE "Submarine landslides and their impacts on
 707 offshore infrastructures") grant agreement 101022007. The authors would
 708 also like to acknowledge the support from the Research Council of Norway
 709 through its Centers of Excellence funding scheme, project number 262644
 710 Porelab. The computations were performed on High Performance Comput-
 711 ing resources provided by UNINETT Sigma2 - the National Infrastructure
 712 for High Performance Computing and Data Storage in Norway.

713 **Appendix: Equation derivation**

714 Before deriving the governing equation, we define the Lagrangian deriva-
 715 tive for a state variable f as:

$$\frac{D_f f}{Dt} = \frac{\partial f}{\partial t} + \mathbf{U}_f \cdot \nabla f \quad \frac{D_s f}{Dt} = \frac{\partial f}{\partial t} + \mathbf{U}_s \cdot \nabla f \quad (101)$$

we use some definition following [16] as below:

$$-\frac{1}{V} \left[\frac{\partial V_f}{\partial p} \right] \equiv \kappa_f \quad \text{isothermal compressibility of fluid} \quad (102)$$

$$\frac{1}{V} \left[\frac{\partial V_f}{\partial T} \right] \equiv \alpha_f \quad \text{constant pressure thermal expansivity of fluid} \quad (103)$$

716 Then, the rate of volume with incompressible solid grains are calculated as
 717 belowbelow:

$$\frac{1}{V} \frac{D_f V_f}{Dt} = \frac{1}{V} \left(\left[\frac{\partial V_f}{\partial p} \right] \frac{D_f P_{eq}}{Dt} + \left[\frac{\partial V_f}{\partial T_f} \right] \frac{D_f T_f}{Dt} \right) = \frac{1}{V} \left(-\kappa_f \frac{D_f P_{eq}}{Dt} + \alpha_f \frac{D_f T_f}{Dt} \right) \quad (104)$$

718 *Evolution of porosity*

719 Solving the solid mass balance equation (4) with the definition of solid
 720 mass in equation (2), it leads to the rate of porosity as belowbelows:

$$\frac{D_s m_s}{Dt} = \frac{D_s(\phi_s \rho_s V)}{Dt} = \rho_s V \frac{D_s \phi_s}{Dt} + \phi_s V \frac{D_s \rho_s}{Dt} + \phi_s \rho_s \frac{D_s V}{Dt} = 0 \quad (105)$$

721 The soil grains are assumed to be incompressible, therefore, term 2 in the
 722 right hand side is zero. leading to:

$$V \frac{D_s \phi_s}{Dt} + \phi_s \frac{D_s V}{Dt} = 0 \quad (106)$$

723 Dividing all terms with V with the equation $\frac{1}{V} \frac{D_s V}{Dt} = \nabla \cdot \mathbf{U}_s$, it leads to:

$$\frac{D_s n}{Dt} = \frac{\partial n}{\partial t} + \mathbf{U}_s \cdot \nabla n = \phi_s \nabla \cdot \mathbf{U}_s \quad (107)$$

724 *Momentum conservation*

725 The linear momentum balance equationequations for the fluid phases
 726 based on mixture theory isare:

$$\frac{1}{V} \frac{D_f(m_f \mathbf{U}_f)}{Dt} = \nabla \cdot (-\phi_f p_f \mathbf{I}) + \nabla \cdot \boldsymbol{\tau}_f + \bar{\rho}_f \mathbf{b} + \sum \mathbf{f}_d + \mathbf{f}_b \quad (108)$$

728 On the right hand sand, the first term is the divergence of partial fluid phase
 729 stress, the third term is the body force, the fourth term is the drag force
 730 (momentum exchange) and the fifth term is the buoyant force described in
 731 [29] for the immiscible mixtures. The buoyant force is in the form asbelows:

$$\mathbf{f}_b = \boldsymbol{\sigma}_f \nabla(n) \quad (109)$$

733 As a result, the linear momentum balance equationequations for the fluid
 734 phases beeomesbecome as:

$$\frac{1}{V} \frac{D_f(m_f \mathbf{U}_f)}{Dt} = \frac{1}{V} \left[\frac{\partial(m_f \mathbf{U}_f)}{\partial t} + \nabla \cdot (m_f \mathbf{U}_f \mathbf{U}_f) \right] = -\phi_f \nabla p_f + \nabla \cdot \boldsymbol{\tau}_f + \bar{\rho}_f \mathbf{b} + \sum \mathbf{f}_d \quad (110)$$

735 The Reynolds stress component can be included in the term $\boldsymbol{\tau}_f$ to consider the
 736 turbulent effects if needed. To derive the linear momentum balance equation

⁷³⁷ for the solid phase, we begin with the linear momentum balance equation for
⁷³⁸ the mixture as:

$$\frac{1}{V} \frac{D_f(m_f \mathbf{U}_f)}{Dt} + \frac{1}{V} \frac{D_s(m_s \mathbf{U}_s)}{Dt} = \nabla \cdot (\boldsymbol{\sigma}) + \bar{\rho}_f \mathbf{b} + \bar{\rho}_s \mathbf{b} \quad (111)$$

⁷³⁹ Combining Terzaghi's equation (3) and subtracting both sides with equation
⁷⁴⁰ (110), we obtain the linear momentum balance ~~equation~~-equations for the
⁷⁴¹ solid phase as:

$$\frac{1}{V} \frac{D_s(m_s \mathbf{U}_s)}{Dt} = \nabla \cdot (\boldsymbol{\sigma}') - \phi_s \nabla p_f + \bar{\rho}_s \mathbf{b} - \sum \mathbf{f}_d + \sum \mathbf{f}_{fric} \quad (112)$$

⁷⁴² Here the \mathbf{f}_{fric} stems from the soil-structure interaction following the contact
⁷⁴³ law between the soil/structure ~~interaces~~interfaces.

⁷⁴⁴ Energy conservation

⁷⁴⁵ We adopt the general form of the total energy balance equation for the
⁷⁴⁶ porous media from [30], the total energy balance equations for the fluid phases
⁷⁴⁷ are:

$$\frac{1}{V} \frac{D_f(m_f(e_f + 0.5 \mathbf{U}_f^2))}{Dt} = \nabla \cdot (-np_f \mathbf{I}) \cdot \mathbf{U}_f + \nabla \cdot \mathbf{q}_f + (\bar{\rho}_f \mathbf{b}) \cdot \mathbf{U}_f + \sum \mathbf{f}_d \cdot \mathbf{U}_f + \sum q_{sf} \quad (113)$$

⁷⁴⁸ Applying the product rule $D(m\mathbf{U}^2) = D(m\mathbf{U} \cdot \mathbf{U}) = 2\mathbf{U} \cdot D(m\mathbf{U})$, the left
⁷⁴⁹ hand side of equation (113) becomes:

$$\frac{1}{V} \frac{D_f(m_f(e_f + 0.5 \mathbf{U}_f^2))}{Dt} = \frac{1}{V} \frac{D_f(m_f e_f)}{Dt} + \frac{1}{V} \frac{D_f(m_f \mathbf{U}_f)}{Dt} \cdot \mathbf{U}_f \quad (114)$$

⁷⁵¹ Combining equations (110), (113), (114), we obtain the final form of the
⁷⁵² internal energy balance equation for the fluid phases as:

$$\frac{1}{V} \frac{D_f(m_f e_f)}{Dt} = \frac{1}{V} \left[\frac{\partial(m_f e_f)}{\partial t} + \nabla \cdot (m_f e_f \mathbf{U}_f) \right] = \bar{\rho}_f p_f \frac{D_f v_f}{Dt} + \nabla \cdot \mathbf{q}_f + \sum q_{sf} \quad (115)$$

⁷⁵³ On the right hand side, the terms include the average pressure-volume work,
⁷⁵⁴ the average viscous dissipation, the thermal transport and the energy ex-
⁷⁵⁵ change between solid and fluid respectively. The heat flux is $\mathbf{q}_f = \bar{\rho}_f \beta_f \nabla T_f$
⁷⁵⁶ with β_f being the thermal conductivity coefficient. To derive the internal
⁷⁵⁷ energy balance equation for the solid phase, we introduce the rate of the

758 internal energy for the thermoelastic materials as a function of elastic strain
 759 tensor $\boldsymbol{\epsilon}_s^e$ and temperature T_s as belows:

$$\frac{m_s}{V} \frac{D_s(e_s)}{Dt} = \boldsymbol{\sigma}' : \frac{D_s(\boldsymbol{\epsilon}_s^e)}{Dt} + \frac{D_s(e_s)}{D_s(T_s)} \frac{D_s(T_s)}{Dt} = \boldsymbol{\sigma}' : \frac{D_s(\boldsymbol{\epsilon}_s^e)}{Dt} + c_v \frac{D_s(T_s)}{Dt} \quad (116)$$

760 c_v is the specific heat at the constant volume of the solid materials. The total
 761 energy balance equation for the mixture based on [30] can be written as:

$$\begin{aligned} \frac{1}{V} \frac{D_f(m_f(e_f + 0.5\mathbf{U}_f^2))}{Dt} + \frac{1}{V} \frac{D_s(m_s(e_s + 0.5\mathbf{U}_s^2))}{Dt} &= \nabla \cdot (-\phi_f p_f \mathbf{I}) \cdot \mathbf{U}_f \\ &+ \nabla \cdot (\boldsymbol{\sigma}' - \phi_s p_f \mathbf{I}) \cdot \mathbf{U}_s + (-\phi_f p_f \mathbf{I}) : \nabla \mathbf{U}_f + \boldsymbol{\sigma}' : \nabla \mathbf{U}_s \\ &+ (\bar{\rho}_f \mathbf{b}) \cdot \mathbf{U}_f + (\bar{\rho}_s \mathbf{b}) \cdot \mathbf{U}_s + \nabla \cdot \mathbf{q}_f + \nabla \cdot \mathbf{q}_s + \sum \mathbf{f}_d \cdot (\mathbf{U}_f - \mathbf{U}_s) \end{aligned} \quad (117)$$

763 Subtracting equation (117), (116) to equations (113) and (112), we obtained
 764 the internal energy balance equation for solid phase as:

$$\boldsymbol{\sigma}' : \frac{D_s(\boldsymbol{\epsilon}_s^e)}{Dt} + \frac{m_s}{V} c_v \frac{D_s(T_s)}{Dt} = \Delta W_s + \Delta W_{friction} + \nabla \cdot \mathbf{q}_s - \sum q_{sf} \quad (118)$$

765 On the right hand side, the terms include the work rate from frictional sliding
 766 between solid materials $\Delta W_{friction}$, thermal transport and energy exchange
 767 between solid and fluid respectively. The heat flux is $\mathbf{q}_s = \bar{\rho}_s \beta_s \nabla T_s$ with β_s
 768 being the thermal conductivity of the solid materials, the mechanical work
 769 rate $\Delta W_s = \boldsymbol{\sigma}' : \frac{D_s(\boldsymbol{\epsilon}_s^e)}{Dt} = \boldsymbol{\sigma}' : (\frac{D_s(\boldsymbol{\epsilon}_s^e)}{Dt} + \frac{D_s(\boldsymbol{\epsilon}_s^p)}{Dt})$ computed from the constitutive
 770 model with $\boldsymbol{\epsilon}_s^p$ is the plastic strain tensor, . By subtracting the term $\boldsymbol{\sigma}' : \frac{D_s(\boldsymbol{\epsilon}_s^e)}{Dt}$,
 771 we get the final form of the energy balance equation as:

$$\frac{m_s}{V} c_v \frac{D_s(T_s)}{Dt} = \boldsymbol{\sigma}' : \frac{D_s(\boldsymbol{\epsilon}_s^p)}{Dt} + \Delta W_{friction} + \nabla \cdot \mathbf{q}_s - \sum q_{sf} \quad (119)$$

772 Advanced Fluid Pressure

773 The discretization of the pressure equation begins with the Lagrangian
 774 face-centered cell face velocity and the equation for the pressure as:

$$\bar{\rho}_{f,FC} \frac{\mathbf{U}_{f,FC}^{n+1} - \mathbf{U}_{f,FC}^n}{dt} = n \nabla^{FC} P_{\textcolor{red}{fc}\textcolor{blue}{f,c}}^{n+1} + \bar{\rho}_{f,FC} \mathbf{b} \quad (120)$$

775

$$\kappa \frac{dP}{dt} = \nabla^c \cdot \mathbf{U}_{f,FC}^{n+1} \quad (121)$$

776 The divergence of the equation (120) with $\nabla \cdot \mathbf{b} = 0$ is:

$$\nabla^c \cdot \mathbf{U}_{f,FC}^{n+1} - \nabla^c \cdot \mathbf{U}_{f,FC}^n = \nabla^c \frac{\Delta t}{\rho_{f,FC}^n} \cdot \nabla^{FC} (P_{fc,fc}^n + \Delta P_{fc,fc}^n) \quad (122)$$

777 To solve this equation, we define the ~~face-centered-cell face~~ intermediate
778 velocity $\mathbf{U}_{f,FC}^*$ as:

$$\bar{\rho}_{f,FC} \frac{\mathbf{U}_{f,FC}^* - \mathbf{U}_{f,FC}^n}{\Delta t} = n \nabla^{FC} P_{fc,fc}^n + \bar{\rho}_{f,FC} \mathbf{b} \quad (123)$$

779 The divergence of the equation (123) is:

$$\nabla^c \cdot \mathbf{U}_{f,FC}^* - \nabla^c \cdot \mathbf{U}_{f,FC}^n = \nabla^c \frac{\Delta t}{\rho_{f,FC}^n} \cdot \nabla^{FC} P_{fc,fc}^n \quad (124)$$

780 Combining equations (121, 122, 124), it leads to:

$$\left(\kappa - \nabla^c \frac{\Delta t}{\rho_{f,FC}^n} \cdot \nabla^{FC} \right) \Delta P_{fc}^n = -\nabla^c \cdot \mathbf{U}_{f,FC}^* \quad (125)$$

781 When the fluid is incompressible, κ approaches to zero and the equation
782 (125) becomes the Poisson's equation for the incompressible fluid flow.

783 *Momentum and Energy exchange with an implicit solver*

784 Considering the fluid momentum balance equation as:

$$(m\mathbf{U})_{f,FC}^{n+1} = (m\mathbf{U})_{f,FC}^n - \Delta t (Vn \nabla^{FC} P_{fc,fc}^n + m_f \mathbf{b}) + VK \Delta t (\mathbf{U}_{s,FC}^{n+1} - \mathbf{U}_{f,FC}^{n+1}) \quad (126)$$

785 Assuming And assuming $m_{f,FC}^{n+1} = m_{f,FC}^n$ we get, we get:

$$\mathbf{U}_{f,FC}^{n+1} = \mathbf{U}_{f,FC}^n - \Delta t \left(\frac{\nabla^{FC} P_{fc}^n}{\rho_{f,FC}^n} + \mathbf{b} \right) + \frac{\Delta t K}{\rho_{f,FC}^n} (\mathbf{U}_{s,FC}^{n+1} - \mathbf{U}_{f,FC}^{n+1}) \quad (127)$$

786 As defined in the section 'Advanced Fluid Pressure', the ~~face-centered-cell~~
787 ~~face~~ intermediate fluid velocity $\mathbf{U}_{f,FC}^* = \Delta t (\nabla^{FC} P_{fc}^n / \rho_{f,FC}^n + \mathbf{b})$ leading to is
788 computed as:

$$\mathbf{U}_{f,FC}^{n+1} = \mathbf{U}_{f,FC}^* + \frac{\Delta t K}{\rho_{f,FC}^n} (\mathbf{U}_{s,FC}^{n+1} - \mathbf{U}_{f,FC}^{n+1}) \quad (128)$$

789 Considering the solid momentum balance equation as:

$$(m\mathbf{U})_{s,FC}^{n+1} = (m\mathbf{U})_{s,FC}^n - \Delta t(V\nabla^{FC} \cdot \boldsymbol{\sigma}'^n - V(1-n)\nabla^{FC}P_{fc,fc}^n + m_s\mathbf{b}) - VK\Delta t(\mathbf{U}_{s,FC}^{n+1} - \mathbf{U}_{f,FC}^{n+1}) \quad (129)$$

790 We define the face-centered cell face intermediate solid velocity as $\mathbf{U}_{s,FC}^* = \Delta t(\nabla^{FC} \cdot \boldsymbol{\sigma}_c'^n / \bar{\rho}_{s,FC} - \nabla^{FC}P_{f,fc}^n / \rho_s + \mathbf{b})$
 791 leading to $\mathbf{U}_{s,FC}^* = \Delta t(\nabla^{FC} \cdot \boldsymbol{\sigma}_c'^n / \bar{\rho}_{s,FC} - \nabla^{FC}P_{f,fc}^n / \rho_s + \mathbf{b})$ leading to:

$$\mathbf{U}_{s,FC}^{n+1} = \mathbf{U}_{s,FC}^* - \frac{\Delta t K}{\bar{\rho}_{s,FC}^n} (\mathbf{U}_{s,FC}^{n+1} - \mathbf{U}_{f,FC}^{n+1}) \quad (130)$$

792 Combining equation (128) and (130) we get:

$$\begin{aligned} \mathbf{U}_{f,FC}^* + \Delta\mathbf{U}_{f,FC} &= \mathbf{U}_{f,FC}^* + \frac{\Delta t K}{\bar{\rho}_{f,FC}^n} (\mathbf{U}_{s,FC}^* + \Delta\mathbf{U}_{s,FC} - \mathbf{U}_{f,FC}^* - \Delta\mathbf{U}_{f,FC}) \\ \mathbf{U}_{s,FC}^* + \Delta\mathbf{U}_{s,FC} &= \mathbf{U}_{s,FC}^* - \frac{\Delta t K}{\bar{\rho}_{s,FC}^n} (\mathbf{U}_{s,FC}^* + \Delta\mathbf{U}_{s,FC} - \mathbf{U}_{f,FC}^* - \Delta\mathbf{U}_{f,FC}) \end{aligned} \quad (131)$$

793 Rearranging the equation (131), it leads to the linear system of equations as
 794 belows:

$$\begin{vmatrix} (1 + \beta_{12,FC}) & -\beta_{12,FC} \\ -\beta_{21,FC} & (1 + \beta_{21,FC}) \end{vmatrix} \begin{vmatrix} \Delta\mathbf{U}_{f,FC} \\ \Delta\mathbf{U}_{s,FC} \end{vmatrix} = \begin{vmatrix} \beta_{12,FC}(\mathbf{U}_{s,FC}^* - \mathbf{U}_{f,FC}^*) \\ \beta_{21,FC}(\mathbf{U}_{f,FC}^* - \mathbf{U}_{s,FC}^*) \end{vmatrix}$$

795 Solving this linear equations with $\beta_{12,FC} = (\Delta t K) / \bar{\rho}_{f,FC}^n$ and $\beta_{21,FC} = (\Delta t K) / \bar{\rho}_{s,FC}^n$ with K is the momentum exchange coefficient. Similar derivation can be performed to computed the cell-center velocity increment leading to:

$$\begin{vmatrix} (1 + \beta_{12c}) & -\beta_{12c} \\ -\beta_{21c} & (1 + \beta_{21c}) \end{vmatrix} \begin{vmatrix} \Delta\mathbf{U}_{fc,fc} \\ \Delta\mathbf{U}_{sc} \end{vmatrix} = \begin{vmatrix} \beta_{12c}(\mathbf{U}_{sc}^* - \mathbf{U}_{fc,fc}^*) \\ \beta_{21c}(\mathbf{U}_{fc,fc}^* - \mathbf{U}_{sc}^*) \end{vmatrix}$$

799 with $\beta_{12c} = (\Delta t K) / \bar{\rho}_{fc}^n$, $\beta_{12c} = (\Delta t K) / \bar{\rho}_{fc}^n$ and $\beta_{21c} = (\Delta t K) / \bar{\rho}_{sc}^n$ and the
 800 cell-centered intermediate velocity can be calculated by:

$$\begin{aligned} \mathbf{U}_{fc,fc}^* &= \mathbf{U}_{fc,fc}^n + \Delta t \left(-\frac{\nabla P_{fc}^{n+1}}{\bar{\rho}_{fc}^n} \frac{\nabla P_{f,fc}^{n+1}}{\bar{\rho}_{f,fc}^n} + \frac{\nabla \cdot \boldsymbol{\tau}_{fc}^n}{\bar{\rho}_{fc}^n} \frac{\nabla \cdot \boldsymbol{\tau}_{f,fc}^n}{\bar{\rho}_{f,fc}^n} + \mathbf{b} \right) \\ \mathbf{U}_{sc}^* &= \mathbf{U}_{sc}^n + \Delta t \left(\frac{\nabla \cdot \boldsymbol{\sigma}_c'^n}{\bar{\rho}_{sc}^n} - \frac{\nabla P_{fc}^{n+1}}{\bar{\rho}_s} \frac{\nabla P_{f,fc}^{n+1}}{\bar{\rho}_s} + \mathbf{b} \right) \end{aligned} \quad (132)$$

801 For generalize multi materials i,j = 1:N, the linear equations is in the form
802 as:

$$\begin{vmatrix} (1 + \beta_{ij}) & -\beta_{ij} \\ -\beta_{ji} & (1 + \beta_{ji}) \end{vmatrix} \begin{vmatrix} \Delta \mathbf{U}_i \\ \Delta \mathbf{U}_j \end{vmatrix} = \begin{vmatrix} \beta_{ij}(\mathbf{U}_i^* - \mathbf{U}_j^*) \\ \beta_{ji}(\mathbf{U}_j^* - \mathbf{U}_i^*) \end{vmatrix}$$

803 Similar approach applied for the ernergy exchange term leading to:

$$\begin{vmatrix} (1 + \eta_{ij}) & -\eta_{ij} \\ -\eta_{ji} & (1 + \eta_{ji}) \end{vmatrix} \begin{vmatrix} \Delta T_i \\ \Delta T_j \end{vmatrix} = \begin{vmatrix} \eta_{ij}(T_i^n - T_j^n) \\ \eta_{ji}(T_j^n - T_i^n) \end{vmatrix}$$

804 with η is the energy exchange coefficient.

805 References

- 806 [1] D. Yuk, S. Yim, P.-F. Liu, Numerical modeling of submarine mass-
807 movement generated waves using RANS model, Computers and Geo-
808 sciences 32 (7) (2006) 927–935. doi:10.1016/j.cageo.2005.10.028.
809 URL <https://doi.org/10.1016/j.cageo.2005.10.028>
- 810 [2] S. Glimsdal, J.-S. L'Heureux, C. B. Harbitz, F. Løvholt, The 29th jan-
811 uary 2014 submarine landslide at statland, norway—landslide dynamics,
812 tsunami generation, and run-up, Landslides 13 (6) (2016) 1435–1444.
813 doi:10.1007/s10346-016-0758-7.
814 URL <https://doi.org/10.1007/s10346-016-0758-7>
- 815 [3] S. Abadie, D. Morichon, S. Grilli, S. Glockner, Numerical sim-
816 ulation of waves generated by landslides using a multiple-fluid
817 navier–stokes model, Coastal Engineering 57 (9) (2010) 779–794.
818 doi:10.1016/j.coastaleng.2010.03.003.
819 URL <https://doi.org/10.1016/j.coastaleng.2010.03.003>
- 820 [4] M. Rauter, S. Viroulet, S. S. Gylfadóttir, W. Fellin, F. Løvholt, Granular
821 porous landslide tsunami modelling – the 2014 lake askja flank collapse,
822 Nature Communications 13 (1) (Feb. 2022). doi:10.1038/s41467-022-
823 28296-7.
824 URL <https://doi.org/10.1038/s41467-022-28296-7>
- 825 [5] Q.-A. Tran, W. Sołowski, Generalized interpolation material point
826 method modelling of large deformation problems including strain-
827 rate effects – application to penetration and progressive fail-
828 ure problems, Computers and Geotechnics 106 (2019) 249–265.

- 829 doi:10.1016/j.compgeo.2018.10.020.
830 URL <https://doi.org/10.1016/j.compgeo.2018.10.020>
- 831 [6] T. Capone, A. Panizzo, J. J. Monaghan, SPH modelling of water
832 waves generated by submarine landslides, *Journal of Hydraulic Research*
833 48 (sup1) (2010) 80–84. doi:10.1080/00221686.2010.9641248.
834 URL <https://doi.org/10.1080/00221686.2010.9641248>
- 835 [7] X. Zhang, E. Oñate, S. A. G. Torres, J. Bleyer, K. Krabbenhoft, A
836 unified lagrangian formulation for solid and fluid dynamics and its possi-
837 bility for modelling submarine landslides and their consequences, *Computer
838 Methods in Applied Mechanics and Engineering* 343 (2019) 314–
839 338. doi:10.1016/j.cma.2018.07.043.
840 URL <https://doi.org/10.1016/j.cma.2018.07.043>
- 841 [8] R. Dey, B. C. Hawlader, R. Phillips, K. Soga, Numerical modelling
842 of submarine landslides with sensitive clay layers, *Géotechnique* 66 (6)
843 (2016) 454–468. doi:10.1680/jgeot.15.p.111.
844 URL <https://doi.org/10.1680/jgeot.15.p.111>
- 845 [9] S. Bandara, K. Soga, Coupling of soil deformation and pore fluid flow
846 using material point method, *Computers and Geotechnics* 63 (2015)
847 199–214. doi:10.1016/j.compgeo.2014.09.009.
848 URL <https://doi.org/10.1016/j.compgeo.2014.09.009>
- 849 [10] A. P. Tampubolon, T. Gast, G. Klár, C. Fu, J. Teran, C. Jiang,
850 K. Museth, Multi-species simulation of porous sand and water
851 mixtures, *ACM Transactions on Graphics* 36 (4) (2017) 1–11.
852 doi:10.1145/3072959.3073651.
853 URL <https://doi.org/10.1145/3072959.3073651>
- 854 [11] A. S. Baumgarten, K. Kamrin, A general constitutive model for dense,
855 fine-particle suspensions validated in many geometries, *Proceedings
856 of the National Academy of Sciences* 116 (42) (2019) 20828–20836.
857 doi:10.1073/pnas.1908065116.
858 URL <https://doi.org/10.1073/pnas.1908065116>
- 859 [12] Q.-A. Tran, W. Sołowski, Temporal and null-space filter for the ma-
860 terial point method, *International Journal for Numerical Methods in*

- 861 Engineering 120 (3) (2019) 328–360. doi:10.1002/nme.6138.
 862 URL <https://doi.org/10.1002/nme.6138>
- 863 [13] X. Zheng, F. Pisanò, P. J. Vardon, M. A. Hicks, An explicit stabilised
 864 material point method for coupled hydromechanical problems in two-
 865 phase porous media, Computers and Geotechnics 135 (2021) 104112.
 866 doi:10.1016/j.compgeo.2021.104112.
 867 URL <https://doi.org/10.1016/j.compgeo.2021.104112>
- 868 [14] Q. A. Tran, W. Sołowski, M. Berzins, J. Guilkey, A convected particle
 869 least square interpolation material point method, International Journal
 870 for Numerical Methods in Engineering 121 (6) (2019) 1068–1100.
 871 doi:10.1002/nme.6257.
 872 URL <https://doi.org/10.1002/nme.6257>
- 873 [15] J.-S. Chen, M. Hillman, S.-W. Chi, Meshfree methods: Progress made
 874 after 20 years, Journal of Engineering Mechanics 143 (4) (Apr. 2017).
 875 doi:10.1061/(asce)em.1943-7889.0001176.
 876 URL [https://doi.org/10.1061/\(asce\)em.1943-7889.0001176](https://doi.org/10.1061/(asce)em.1943-7889.0001176)
- 877 [16] B. A. Kashiwa, A multifield model and method for fluid-structure in-
 878 teraction dynamics, Tech. Rep. LA-UR-01-1136, Los Alamos National
 879 Laboratory (2001).
- 880 [17] J. Guilkey, T. Harman, B. Banerjee, An eulerian–lagrangian
 881 approach for simulating explosions of energetic devices,
 882 Computers and Structures 85 (11) (2007) 660 – 674.
 883 doi:<https://doi.org/10.1016/j.compstruc.2007.01.031>.
 884 URL <http://www.sciencedirect.com/science/article/pii/S0045794907000429>
- 885 [18] A. S. Baumgarten, B. L. Couchman, K. Kamrin, A coupled finite volume
 886 and material point method for two-phase simulation of liquid–sediment
 887 and gas–sediment flows, Computer Methods in Applied Mechanics and
 888 Engineering 384 (2021) 113940. doi:10.1016/j.cma.2021.113940.
 889 URL <https://doi.org/10.1016/j.cma.2021.113940>
- 890 [19] S. Bardenhagen, J. Guilkey, K. Roessig, J. Brackbill, W. Witzel,
 891 J.C.Foster, An improved contact algorithm for the material point
 892 method and application to stress propagation in granular material,

- 893 CMES-Computer Modeling in Engineering and Sciences 2 (2001) 509–
894 522. doi:10.3970/cmes.2001.002.509.
- 895 [20] J. A. M. K. R. Beetstra, M. A. van der Hoef, Drag force of intermediate
896 reynolds number flow past mono- and bidisperse arrays of spheres,
897 Fluid Mechanics and Transport Phenomena 53 (2) (2007) 489 – 501.
898 doi:<https://doi.org/10.1002/aic.11065>.
- 899 [21] R. W. Stewart, The air-sea momentum exchange, Boundary-Layer Me-
900 teorology 6 (1-2) (1974) 151–167. doi:10.1007/bf00232481.
901 URL <https://doi.org/10.1007/bf00232481>
- 902 [22] S. G. Bardenhagen, E. M. Kober, The generalized interpolation material
903 point method, Computer Modeling in Engineering and Sciences 5 (2004)
904 477–496. doi:10.1016/j.compgeo.2021.104199.
905 URL <https://doi.org/10.3970/cmes.2004.005.477>
- 906 [23] S. G. Amiri, E. Taheri, A. Lavasan, A hybrid finite element model for
907 non-isothermal two-phase flow in deformable porous media, Computers
908 and Geotechnics 135 (2021) 104199. doi:10.1016/j.compgeo.2021.104199.
909 URL <https://doi.org/10.1016/j.compgeo.2021.104199>
- 910 [24] S. A. R. C. Mariotti;, P. Heinrich, Numerical simulation of sub-
911 marine landslides and their hydraulic effects, Journal of Wa-
912 terway, Port, Coastal, and Ocean Engineering 123 (4) (1997).
913 doi:[https://doi.org/10.1061/\(ASCE\)0733-950X\(1997\)123:4\(149\).](https://doi.org/10.1061/(ASCE)0733-950X(1997)123:4(149).)
- 914 [25] A. Alsardi, A. Yerro, Runout Modeling of Earthquake-Triggered
915 Landslides with the Material Point Method, pp. 21–31.
916 arXiv:<https://ascelibrary.org/doi/pdf/10.1061/9780784483428.003>,
917 doi:10.1061/9780784483428.003.
918 URL <https://ascelibrary.org/doi/abs/10.1061/9780784483428.003>
- 919 [26] H. N., O. A., B. H. H., R. P., R. Fukagawa, Seismic slope failuremod-
920 elling using the mesh-free sph method, International Journal of Geomate
921 (2013) 660–665.
- 922 [27] T. Bhandari, F. Hamad, C. Moormann, K. Sharma,
923 B. Westrich, Numerical modelling of seismic slope failure us-
924 ing mpm, Computers and Geotechnics 75 (2016) 126–134.

- 925 doi:<https://doi.org/10.1016/j.compgeo.2016.01.017>.
926 URL <https://www.sciencedirect.com/science/article/pii/S0266352X16000264>
- 927 [28] D. Muir Wood, Soil behaviour and critical state soil mechanics, Cam-
928 bridge University Press, United Kingdom, 1990.
- 929 [29] D. Drumheller, On theories for reacting immiscible mixtures, Inter-
930 national Journal of Engineering Science 38 (3) (2000) 347 – 382.
931 doi:[https://doi.org/10.1016/S0020-7225\(99\)00047-6](https://doi.org/10.1016/S0020-7225(99)00047-6).
932 URL <http://www.sciencedirect.com/science/article/pii/S0020722599000476>
- 933 [30] S. Hassanzadeh, Derivation of basic equations of mass transport in
934 porous media, part1: Macroscopic balance laws, Advances in Wa-
935 ter Resources 9 (1986) 196–206. doi:[https://doi.org/10.1016/0309-1708\(86\)90024-2](https://doi.org/10.1016/0309-1708(86)90024-2).